TERRESTRIAL INVESTIGATION OF VAPOR BUBBLE CHARACTERISTICS IN NUCLEATE POOL BOILING OF A DIELECTRIC FLUID ON AN ASYMMETRIC MICROSTRUCTURED METAL HEAT SINK (PRE-CURSOR TO MICROGRAVITY ISS EXPERIMENTS)

by

Karthekeyan Sridhar

A thesis submitted to the Graduate Faculty of
Auburn University
in partial fulfillment of the
requirements for the Degree of
Master of Science

Auburn, Alabama
August 8, 2020

Keywords: Two-phase, Microstructured surface, Passive pumping,
Bubble dynamics, Electronic Thermal Management.

Approved by

Sushil H. Bhavnani, Professor, Mechanical Engineering
Roy W. Knight, Associate Professor, Mechanical Engineering
Nicholas Tsolas, Assistant Professor, Mechanical Engineering

Abstract

This experimental, terrestrial study is part of a larger effort to dissipate increased heat fluxes through enhanced pool boiling in spacecraft electronics prior to an extensive study to be conducted on the International Space Station under pristine microgravity conditions. The absence of buoyancy forces in microgravity causes vapor bubbles to grow to a very large size, leading to premature critical heat flux (CHF). Using an engineered surface modification, namely an asymmetric sawtooth ratchet, to create mobility of the vapor mass can alleviate this problem. The stainless steel (SS 316L) test surfaces were fabricated using powder bed fusion, a metal additive manufacturing process. Boiling experiments were conducted in the upward-facing and downward-facing orientations in the designed terrestrial setup. Apart from the surface orientation, parameters such as cavity density (1-mm or 2-mm apart), sawtooth structure (60°-30° or 75°-15°) were also studied. The downward-facing orientation explored in this study is the bridge between the terrestrial and microgravity experiments, as buoyancy forces do not detach vapor bubbles from the surface. Vapor mobility was observed in the downward-facing configuration for the asymmetric sawtooth structure explored in the study. A thin liquid film was observed between the microstructure and vapor bubbles as they slid along the microstructure. The non-uniform nature of this liquid film is explored using high-speed imaging at the crest and trough of the sawtooth. A model to predict liquid film thickness for the downward-facing surface is proposed, based on modifications from a previous NASA Zero-G flight model. The proposed asymmetric saw-tooth microstructure is a potential technique to induce motion of vapor bubbles across electronic components when reduced buoyancy forces do not detach vapor bubbles from the surface.

Acknowledgements

To my committee members Dr. Sushil H. Bhavnani, Dr. Roy W. Knight and Dr. Nicholas Tsolas, thank you for reviewing this manuscript and serving on my committee. I would like to especially thank Dr. Sushil Bhavnani for his mentorship, patience, and constant support throughout my research. Thanks to my Auburn friends, Aaron Smith, Le Gao, and Michael Henry, for their support as friends and colleagues.

Thanks to Matt Montgomery for his assistance in fabricating the glass ampoules used in this study.

Finally, I would like to thank my parents and my sister for their confidence, support, and love without whom this work would not have been possible.

Table of Contents

List of Figures

List of Tables

NOMENCLATURE

Acronyms

BXF	Boiling eXperimental Facility
CHF	Critical Heat Flux
CTE	Coefficient of Thermal Expansion
DLD	Direct Laser Deposition
ISS	International Space Station
MSG	Microgravity Science Glovebox
NIST	National Institute of Science and Technology
NPBX	Nucleate Pool Boiling eXperiment
ONB	Onset of Nucleate Boiling
REC	Re-entrant Cavity
RMS	Root Mean Squared
RTV	Room-Temperature-Vulcanizing
SS	Stainless Steel
TEC	Thermoelectric Cooler
TED	Thermoelectric Device
PFMI	Pore Formation and Mobility During Controlled Directional Solidification in a Microgravity Environment Investigation

Symbols

A	area, m^2
D	diameter, m
F	Force, N
G	gravity, m/s^2
H	height, m

I	supply current, A
K	thermal conductivity, W/mK
L	length, m
P	pressure, atm
Q	power supplied to the heater, W
q''	heat flux, W/cm^2
R	radius, m
R	radius of curvature, m
T	temperature, ◦C
v	velocity, m/s
V	voltage, V

Greek symbols

ΔT_{sub}	inlet subcooling, ◦C
μ	dynamic viscosity, Nsm^{-2}
υ	kinematic viscosity, m^2/s
ρ	density, kg/m^3
σ	surface tension, N/m
θ	saw tooth angle, degree

Subscripts

l	liquid
sat	saturation
w	wall
v	vapor

CHAPTER 1 INTRODUCTION

The rapid growth of microelectronic fabrication techniques has led to increasingly compact footprints of processing units, data centers and supercomputers. There are various measures to quantify this development that the semiconductor fabrication industry uses. While the die size is a straightforward unit of measurement, the lithographic node is not well-defined. In the early days of semiconductor fabrication, the lithographic node was defined as the gate length or half-pitch. However, that definition has evolved over time, and now, semiconductor companies prefer to define their node sizes by their own formulas.

However, it is an undeniable fact that transistor sizes have decreased with time according to Moore’s Law as shown in Figure 1. Moore’s law can be defined, roughly, as the expectation that the number of transistors per unit chip area doubles every two years. Due to high transistor density, more computing power can be packed into a smaller footprint leading to higher productivity. Therefore, the number of operations performed per unit area has shot up considerably over the past couple of decades. As higher technology nodes are fabricated, the power consumption, leakage and dissipation from chips is lowered. Moore’s Law also helps the semiconductor fabrication industry to create roadmaps for future decades. For example, from 1971 through 2020, an international document outlined the predictive progress, titled “The International Technology Roadmap for Semiconductors”[1]. This helps the research and development focus its efforts on a two-year cycle.

With microelectronic fabrication heading towards a highly mechanistic understanding to measure error rates in terms of atoms, auxiliary industries supporting this development have also been forced to move towards better process control and predictive capabilities. For example, cooling of electronics has rapidly evolved to keep pace with explosive growth of microelectronics fabrication. Due to form factor shrinkage of devices, highly aggressive cooling methods like phase change of coolants are now mainstream. As the amount of space required to carry out complex calculations has shrunk, the heat flux required to be dissipated from these compact transistors has risen to unprecedented levels. Conventional air-cooling techniques are not sufficient to meet the ever-rising demand of powerful electronics required to perform complex tasks. While liquid cooling systems can be used to dissipate the heat generated, most of these systems required a controlled flow loop with bulky pumps. These systems also drive up the cost required to cool a unit area of electronics. Phase-change systems are feasible alternatives that can dissipate high heat fluxes while also preventing high chip temperatures.

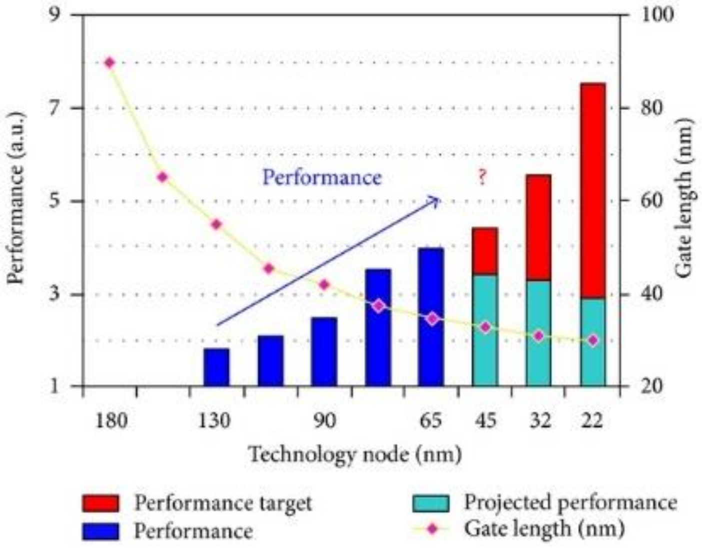

Figure 1: Performance increase from a chip as a function of fabrication length-scale. As performance of the devices increase, the space required to carry out complex calculations has shrunk. [2]

Cooling solutions are harder to design for microgravity systems due to the lack of buoyancy forces. Liquid-vapor phase change solutions depend on mobility of the vapor bubbles to support high heat fluxes. When buoyancy forces become negligible, the vapor bubbles do not detach from the heated surface, leading to an undesirable heat transfer situation. While closed flow loop solutions with pumps and coolants like water and ammonia are feasible (like the solar panel cooling system on the International Space Station [3]), these thermal management techniques do not scale well to device level or chip level footprints. The proposed surface microstructure in this study is a potential technique to slide vapor bubbles across electronic heat sources in microgravity conditions, without the use of pumps or flow loops.

1.1 Pool Boiling

The phenomenon of a heated surface producing boiling in an extensive pool of stationary liquid is referred to as pool boiling. Pool boiling is perhaps the most encountered two-phase heat transfer technique, ranging in applications from metallurgy to electronics cooling. Most features of the pool boiling curve understood today as conventional, mainstream theory was laid out in the seminal work by Nukiyama [4]. Nukiyama provided electrical heating to wires of three different metals like nickel, platinum and nichrome and recorded the power input and subsequent change in surface temperature as shown in Figure 2. He also discussed the burn-out effect, now labeled as the critical heat flux, where the jump in surface temperature was large enough to melt most metals used in the experiment.

While the fundamentals of pool boiling laid out by Nukiyama have been concrete over the past few decades, many attempts to gain a mechanistic understanding of pool boiling have proved elusive. However, some theories on heat transfer enhancement through engineered surfaces have taken center stage over time because of their reproducibility and repeatability across researchers.

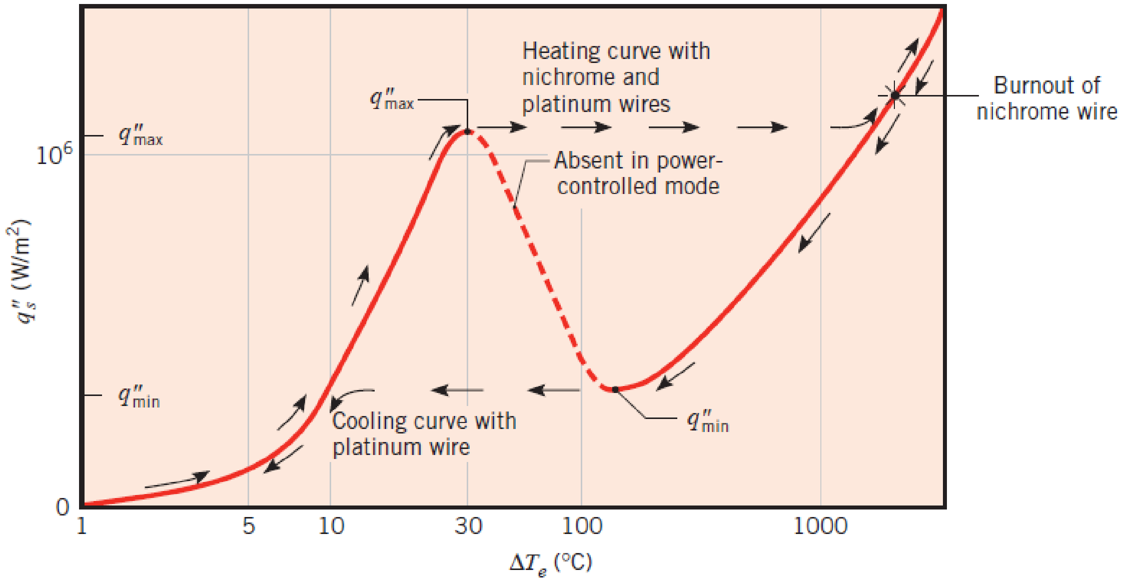

Figure 2: Salient features of the pool boiling curve as explained by Nukiyama for increasing heat flux[5]

1.1.1 Pool Boiling Augmentation

One such popular theory is that of test surface enhancements such as engineered microstructures augmenting pool boiling. Anderson and Mudawar [6] experimentally studied pool boiling enhancement through surfaces with fins, studs, grooves, varying surface roughness and vapor-trapping cavities, as shown in Figure 3, with FC-72 as the test fluid. The engineered surfaces with dimensions of 12.7 x 12.7 mm were vertically oriented and attached to a copper calorimeter bar. The study found that increasing surface roughness resulted in lower required superheat for onset of nucleate boiling, and subsequently led to lower temperature overshoot. The artificial cavity surfaces were varied as perpendicular or inclined indentations into the surface. The results indicated that the inclined cavities improved the critical heat flux (CHF) by 25% due to nucleate pool boiling augmentation. Though cavity sizes were not varied in the study, artificial cavities on the order of 0.3 mm were found to be effective in lowering the wall superheat required for the onset of nucleate pool boiling and led to an increase in critical heat flux. Low profile surface enhancements, or microstructures, were found to be effective in shifting the boiling curve to lower superheats and increased the critical heat flux as well.

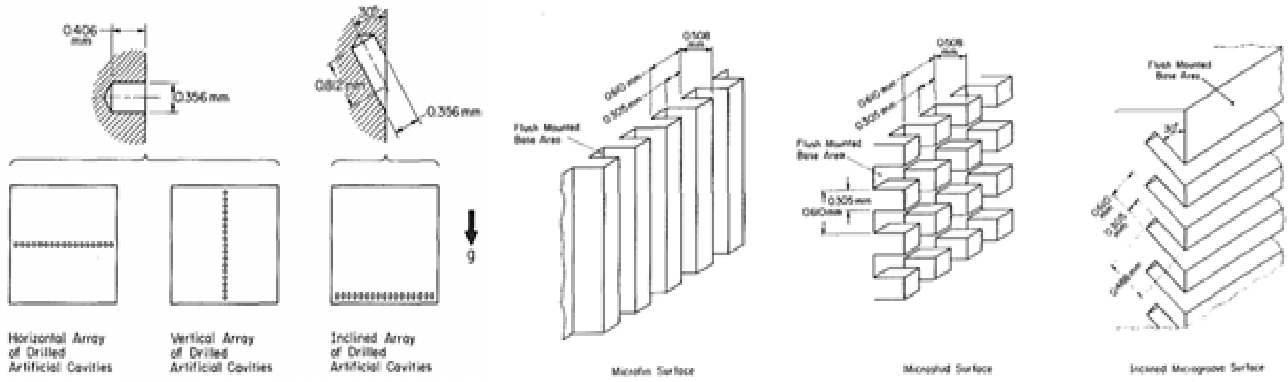

Figure 3: The range of surface enhancements employed including artificial cavity configurations and low-profile surface enhancements [6]

Another popular, well-researched theory states that the cavities in a heated surface serve as the nuclei for initial vapor nucleation due to entrapped gas. This leads to heterogeneous nucleation at lower superheats, thereby enhancing pool boiling heat transfer. An extension of this theory describes that specific kinds of cavities, such as the one shown in Figure 4, called re-entrant cavities, are especially stable due to enhanced thermodynamic stability.

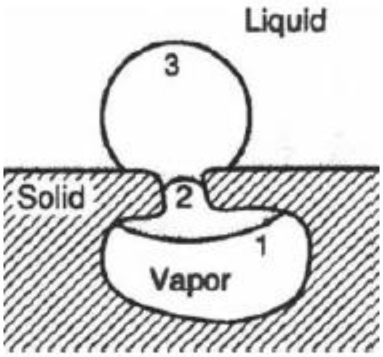

Figure 4: Growth of a bubble from a reentrant cavity as illustrated by Carey [7]

Though a body of theoretical framework applies well-known knowledge of highly wetting fluids and contact angles to describe this ‘super-equilibrium’, the empirical evidence obtained through several studies forms the framework of understanding heterogeneous boiling in line with cavity incipience theory. Rajulu et al. [8] studied the effect of re-entrant cavities on enhancement of the pool boiling heat transfer coefficient using heated tubes. The test fluids used included acetone, isopropanol, ethanol, and water. The profile of the re-entrant cavity and cavity dimension are show in Figure 5. The authors found that an optimum cavity mouth size exists for each test fluid and that the REC-2 tube provided the highest heat transfer enhancement for acetone and isopropanol.

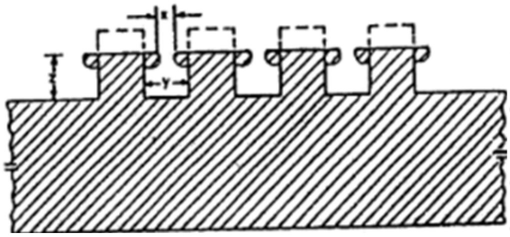

Cavity dimensions	Heating tubes				
	REC-0	REC-1	REC-2	REC-3	REC-4
x	0.50	0.40	0.30	0.25	0.20
y	0.50	0.50	0.50	0.50	0.50
z	0.50	0.50	0.50	0.50	0.50

Figure 5: Profile of the re-entrant cavity (left) along with cavity dimensions (right) used by Rajulu et al. [8]

While the above results suggest that a properly sized re-entrant cavity enhances heat transfer, a surface saturated with many cavities might not necessarily improve boiling characteristics. Nimkar et al. [9] studied the effect of nucleation spacing on the pool boiling characteristics of surface with pyramidal re-entrant cavities with FC-72 as the test fluid. The pyramidal cavity tapered in size from a 40-micron square mouth to a 240-micron square base with nucleation site spacing varying as 0.5 mm, 0.75 mm and 1 mm as shown in Figure 6. Nucleation site density was found to strongly influence pool boiling characteristics with the 0.75 mm spacing surface outperforming the other two. A significant observation from this study concluded that the surface with the lowest spacing between cavities performed worse than the baseline, plain surface. The effect was attributed to repulsive interaction between nucleating cavities and hindered boundary layer mixing. To summarise, the existing literature suggests that engineered microstructures [8–11] and cavities shift the onset of nucleate boiling to lower superheats, and that for each fluid, an optimal cavity mouth size and cavity spacing exists.

1.1.2 Parametric effects on pool boiling

Though several parametric effects of pool boiling have been investigated, the effect of pool boiling within a confined space has only been investigated by a few researchers. Ghiu and Joshi [14] experimentally studied the boiling phenomena from thin, enhanced, confined structures and found that the overall heat transfer performance of a confined test surface was considerably worse compared to the unconfined condition. However, the authors found a range of low heat fluxes ($1\ W/cm^2 < q'' < 4\ W/cm^2$) where the confined, enhanced showed superior heat transfer performance compared to a baseline, plain structure with an open top (unconfined). The effect was attributed to latent heat transport at low heat fluxes.

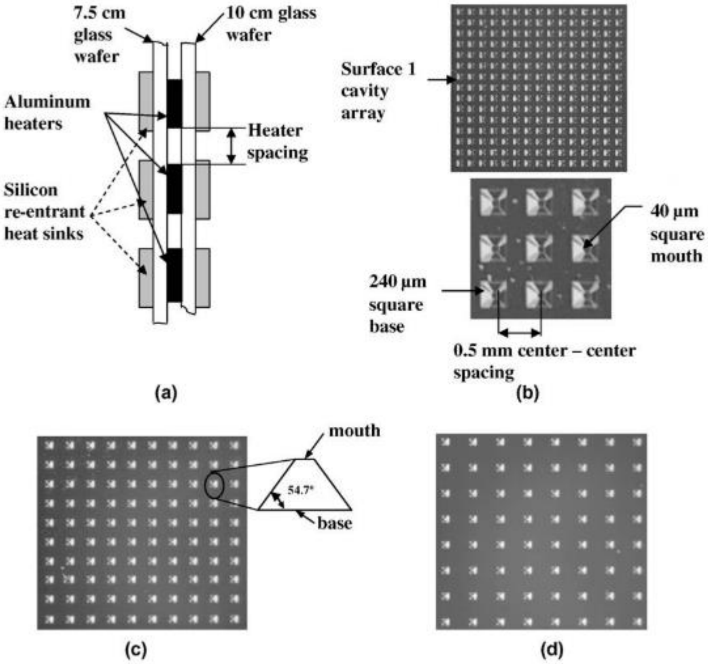

Figure 6: The details of glass substrate along with varying nucleation site spacings utilised by Nimkar [9]

Fujita et al. [15] investigated pool boiling heat transfer in a confined narrow space for saturated water. The confinement effect was studied using two different kinds of periphery: Open periphery and closed periphery. The effect of heating surface inclination was also varied from the vertical to facing downwards nearly to the horizontal. Two heating surfaces, A and B, were held at lengths of 30 mm and 120 mm respectively while their widths were 30 mm. The gap between the heated and unheated plate was varied across 5, 2, 0.6 and 0.25 mm under different periphery conditions, as shown in Figure 7(left). The effect of the surface inclination was studied across three different angles from the horizontal plane $\theta = 90°(vertical), 150°, 175°(downward\ facing\ surface)$.

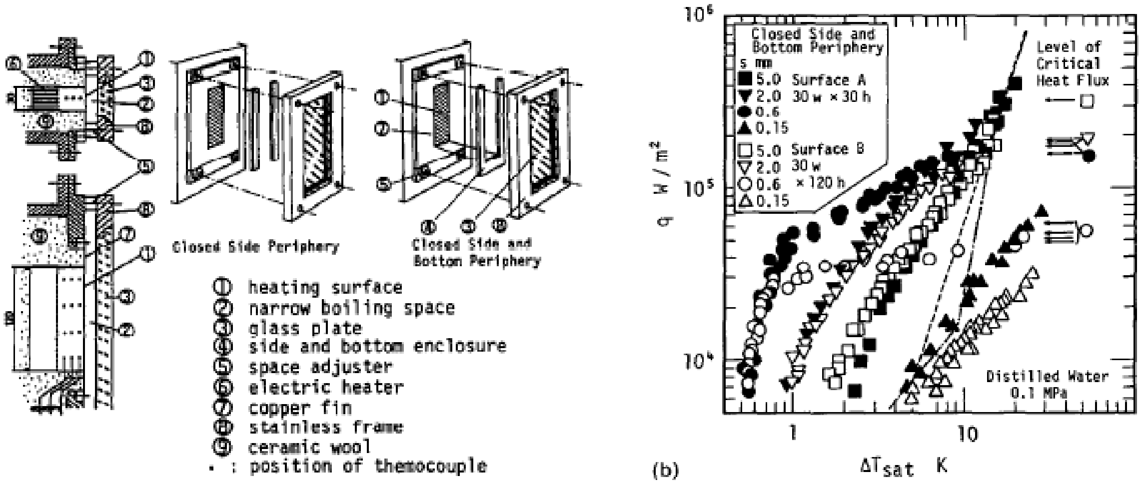

Figure 7: The experimental setup used by Fujita et al. [15] **(left). The effect of heated surface length for closed and open peripheries in the experiment on the boiling curves (right)**

For the vertical orientation under the closed periphery condition (closed side and bottom periphery), the longer surface, B, supported a lower rate of heat transfer than the shorter surface. At higher gap sizes, the effect was distinctively less pronounced. At a gap size of 0.6 mm, the effect of the length held at higher heat fluxes and over the whole heat flux range for a gap of 0.15 mm. The authors reasoned that a combination of the longer surface and narrower gap causes higher vapor velocity at the exit which hinders liquid penetration at the open top edge.

At an inclination of $175°(almost\ downward\ facing\ surface)$ and gap size of 5 mm, the heat transfer is significantly enhanced than that for the vertical surface. The effect is attributed to the flattened bubbles pushing up to the heated surface, leading to an enlarged contact area. This further results in thin liquid film evaporation under these bubbles leading an increased heat transfer rate. At lower gap sizes, the heat transfer rate is poorer due to accumulation of vapor on the heating surface. Heat transfer is enhanced by a downward facing surface at a gap length of 5 mm.

Similar studies with different orientations have been conducted with dielectric fluids. Priarone [16] analysed the effects of surface orientation on a smooth copper surface for two dielectric fluids – FC-72 and HFE-7100. The angle of orientation was varied from $0^{\circ}\ to\ 175^{\circ}$ with regular increments. Boiling curves were plotted until the dry-out point and correlations for CHF and heat transfer were developed as function of inclination angle. For FC-72, in the low-heat-flux nucleate boiling region, the heat transfer coefficient increased markedly with orientation angle; for higher heat flux values, the effect was evident only for angles greater than 90° and the heat transfer coefficient diminished as the angle increased. The critical heat flux CHF decreased slightly as the orientation angle increased from 0 to 90, while for downward-facing surfaces, the CHF decreases rapidly as the orientation angle increased towards 180°. The authors also compared their data with that of Chang-You who used a 1 cm x 1 cm square heater and found that their copper disk with 3 cm diameter performed markedly better.

Rainey et al.[17] conducted a study closely related to that of Chang-You's [18], which studied the enhancement of pool boiling in microporous surfaces against plain surfaces in saturated FC-72. However, this study employed two different heater sizes- 2 cm x 2 cm and 5 cm x 5 cm- and compared it against the 1 cm x 1 cm heater used by Chang-You[18]. While the effects of surface orientation were in line with previous studies, there was no discernible trend against heater size found for the 180° orientation as shown in Table 1.

Table 1: Critical heat flux for the 180° orientation as a function of heater size in Rainey et al.[17]

Heater Size (cm^2)	**CHF (W/cm^2)**
1	1.6
4	0.95
25	2.5

An important drawback of this study might be in not including a data point for a 175° orientation since the boiling crisis is delayed by a preferential direction, as supported by previous authors. However, in the 160° orientation, the CHF shows a steady downward trend with increasing heater size as shown in Table 2.

Table 2: Critical heat flux for 160° orientation as a function of heater size in Rainey et al. [17]

Heater Size (cm^2)	**CHF (W/cm^2)**
1	8.2
4	6.3
25	6.2

The study also points towards a diminishing effect of enhancement as the heater size increases. The effects of surface orientation on pool boiling provide a clear consensus while the effects of heater length/size seem to be conflicted and poorly understood. This is further made difficult due to the inherent problems in comparing across different heater shapes (square vs rectangular vs circular).

1.2 Heat transfer phenomena and bubble dynamics associated with ratcheted microstructures

In the next section of this literature review, the focus is turned towards ratcheted microstructures and the heat transfer phenomena associated with these structures. Early attempts at moving fluid away from a heated surface was primarily studied using the convective flows setup from the surface. In single phase liquids, these effective convective flows are labeled as Marangoni effect and Rayleigh-Benard instability.

When a single-phase liquid is heated, the warmer layers of the liquid rise to the top. As the temperature of the fluid rises, the surface tension decreases due to deteriorating cohesive forces within. This sets up an alternating flow of warm and cold liquid at the liquid-gas interface due to surface tension gradients. The local cellular flow setup by differing surface tension gradients is called the Marangoni effect. Marangoni Bernard convection is depicted in Figure 8.

Jo[19] showed that 60°-30° sawtooth ratchet induced asymmetric net force on a thin layer of silicone oil in the streamwise direction as shown in Figure 9. A small droplet of dye was added to the silicone oil in the closed loop system to track its velocity as it progressed through the loop. It was found that a net flow velocity of ~0.9 m/min was induced by the ratchets in a 1 mm thick silicone oil layer.

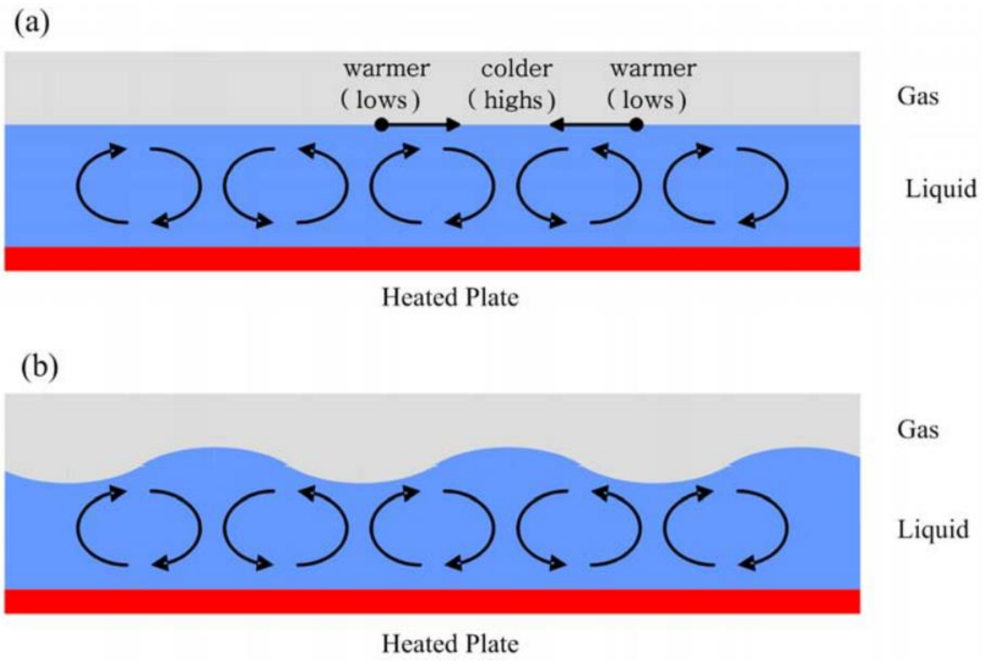

Figure 8: Schematic depiction of the Marangoni Bernard convection setting up the deflection of the gas-liquid interface [19]

The Marangoni number is defined as the ratio of surface tension forces to viscous forces,

$$Ma = \frac{\left(\frac{d\sigma}{dT}\right)\Delta TL}{\alpha\mu}$$

where $\left(\frac{d\sigma}{dT}\right)$ is temperature coefficient of surface tension, ΔT is temperature difference between top surface and bottom surface of the liquid layer, L is thickness of the liquid layer, α is thermal diffusivity, and μ is dynamic viscosity. The Marangoni number was varied by two independent parameters-the surface-to-ambient temperature differential and the liquid-to-ratchet thickness. The oblong flow loop constructed by Jo is depicted in Figure 9. It is worth mentioning here that Stroock et al. [20] introduced the concept of asymmetric ratchets to create Marangoni-Bernard convection in a thin layer of silicone oil to generate net flow.

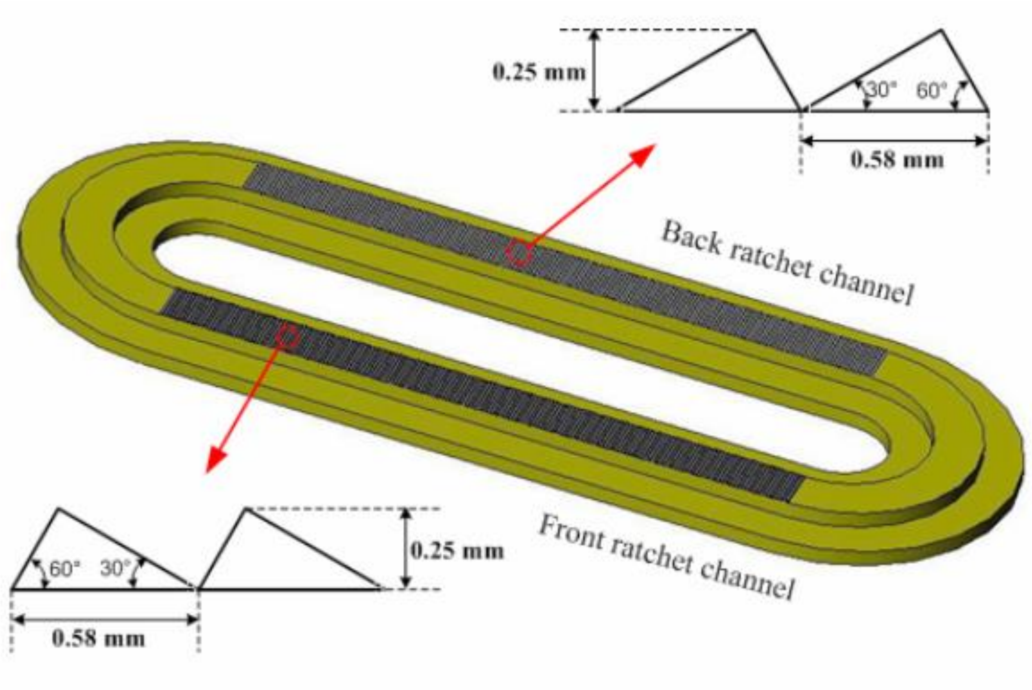

Figure 9: Details of the oblong flow loop constructed with asymmetric ratchets - Jo [19]

Ratchet-like topography has been explored for different regions of the boiling curve by other researchers as well. Linke et al.[21] reported pumping of liquid droplets due to asymmetric brass ratchets in the Leidenfrost regime for multiple liquids including R134a, ethanol and water. Apart from the net force induced by the microstructure, Linke theorized that thermocapillary flow along the ratchet's length away from the wetting point might also be responsible for the net pumping of fluid along the x-direction. The pumping motion of a R134a droplet is illustrated in Figure 10. Dupeux et al. [22] investigated the dominant force inducing motion along the ratchets as reported by Linke and confirmed that the viscous forces induced by the asymmetric flow assumed importance compared to the inertial stresses for the Leidenfrost regime.

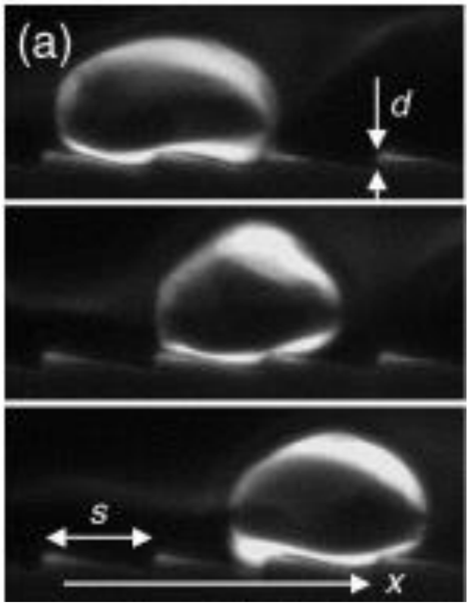

Figure 10: Pumping action of a R134a droplet on brass ratchets observed over a timescale of 32 milliseconds - Linke et al. [21]

Within the context of two-phase heat transfer, Kapsenberg et al. [23] demonstrated liquid motion in excess of 600 mm/s near the heated surface from the ratcheted microstructure, modified with re-entrant cavities on the long slope. A simple, preliminary model based on force balance was developed and validated through an experiment with deionized water.

1.3 Pool boiling in microgravity

Similar discrepancies have also been reported by other microgravity studies across varied experimental methods. The methods of investigation vary across drop towers, parabolic flights, and experiments aboard the International Space Station (ISS). Xue et al. [24] studied nucleate pool boiling of FC-72 on a smooth surface under microgravity utilizing the Beijing drop tower. Two distinct modes of vapor bubble physics was observed depending on the applied heat flux. In the low heat flux region, the bubbles grew to a large diameter but remained attached to the heater surface with little coalescence. In the high heat flux region, the bubble density as well as bubble diameters increased significantly. Smaller bubbles were “sucked” into larger bubbles due to capillary flow near the heater’s surface. The coalescence of smaller bubbles led to departure of the large bubble due to momentum resulting from the coalescing process. An important conclusion from the authors suggested that thermocapillary forces may be an important mechanism helping the bubbles stay attached to the heater surface, aside from the lack of buoyancy forces.

Raj et al. [25] conducted over 200 pool boiling experimental runs in microgravity aboard the ISS using the Boiling eXperiment Facility (BXF). Semi-transparent microheaters were used to enable camera view through the array and bellows were used to maintain the pressure in the chamber between 0.57 atm-2.67 atm. The wall superheat required for onset of nucleate boiling was found to decrease with increasing pressure and were lower compared to 1-g values. At low subcoolings (ΔT_{sub}=1°C), heat transfer attributed to boiling was negligible as the bubble grew to a large size and covered the entire heater by vapor. The authors differentiated boiling in earth gravity and microgravity by describing them as buoyancy dominated boiling and surface tension dominated boiling, respectively. A modified gravity scaling parameter to predict heat flux in microgravity was discussed and verified from the obtained experimental data.

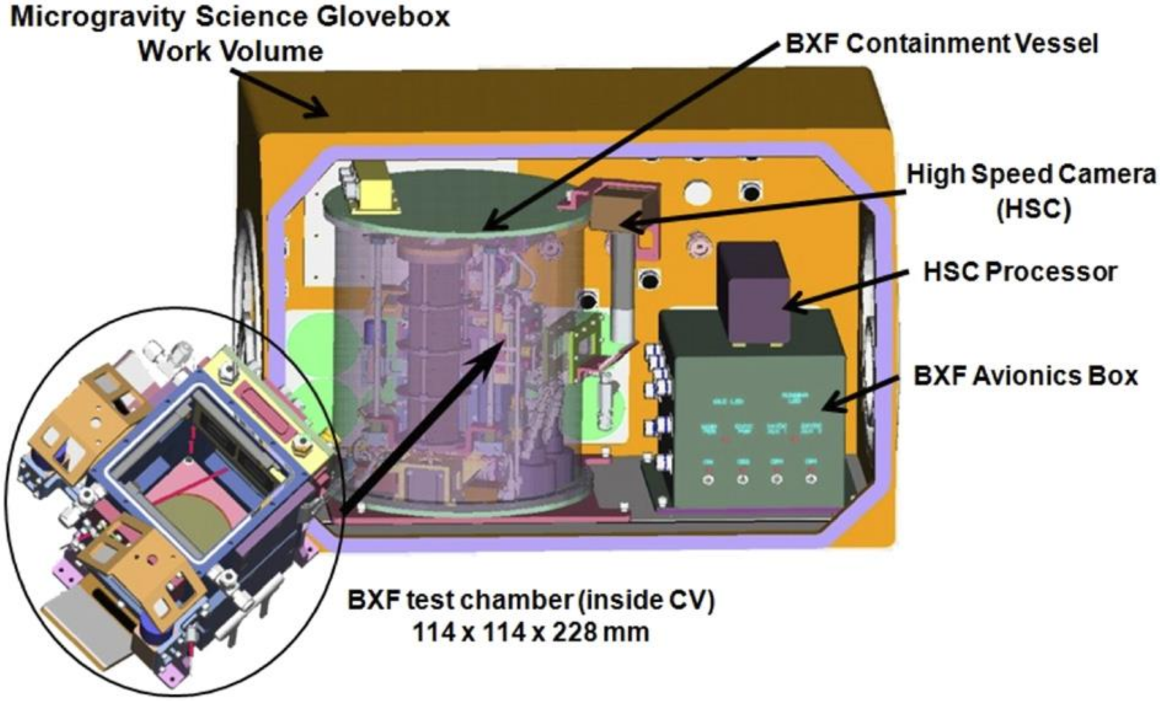

Figure 11: The Boiling eXperimental Facility contained within the Microgravity Science Glovebox with high speed camera and sensors

Warrier et al. [26] studied nucleate pool boiling using a polished aluminum disc with five cylindrical cavities with four cavities placed at the corners of a square and one in the middle, as shown in Figure 12. The apparatus, termed the Nucleate Pool Boiling eXperiment (NPBX), was housed alongside [25]'s setup in the Microgravity Science Glovebox (MSG) aboard the ISS. The fluids used was FC-72, with a similar test setup as [25]'s including bellows and a flow test loop. The study observed that at low wall superheats during the onset of nucleate boiling, nucleated bubbles merged to form a large central bubble in the middle of the square. This large central bubble stayed on the heater surface and grew to a large diameter, as shown in Figure 13. These observations are consistent with the other microgravity studies reported above, where the consensus is that bubbles stayed on the surface and grew to very large diameters. This situation severely inhibits heat transfer from the surface since the large vapor bubble poorly dissipates heat. Therefore, the experimental study of boiling in reduced gravity is essential to facilitate high heat flux cooling of space electronics due to poor heat transfer conditions.

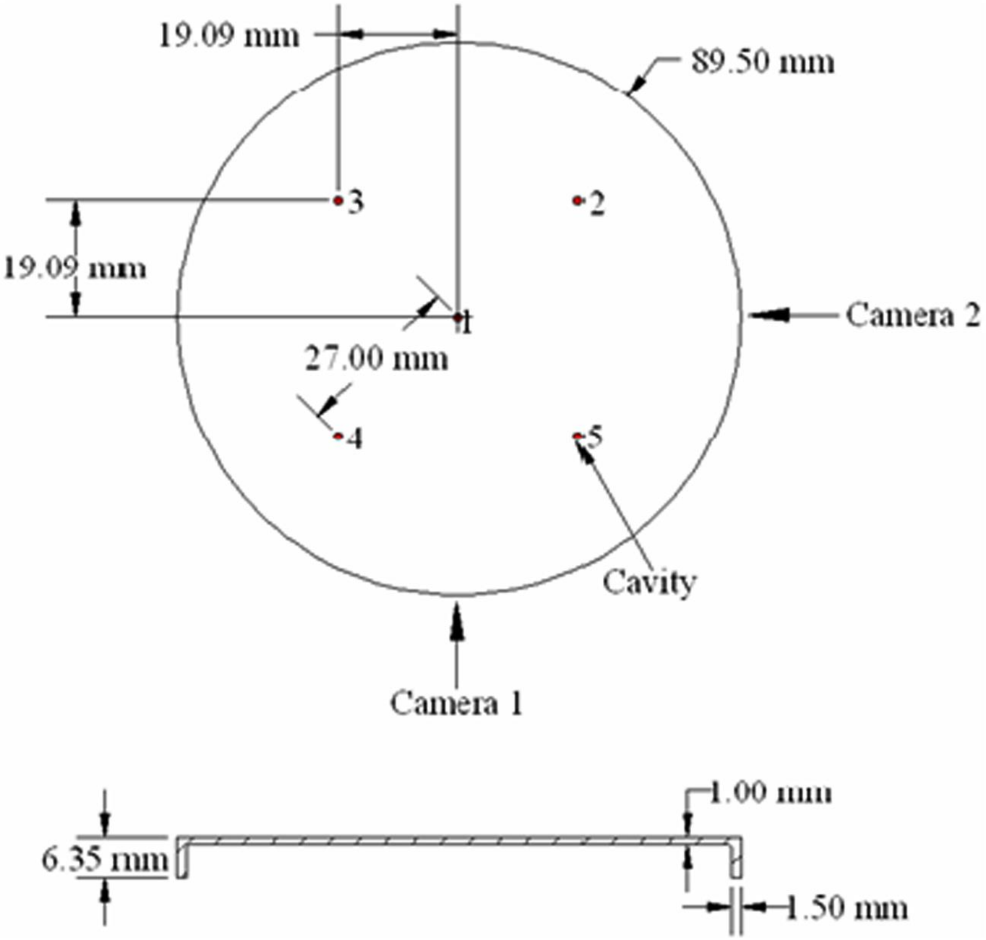

Figure 12: The boiling test surface used in the Nucleate Pool Boiling eXperiments (NPBX) aboard the ISS, complete with details of cavity placement and camera

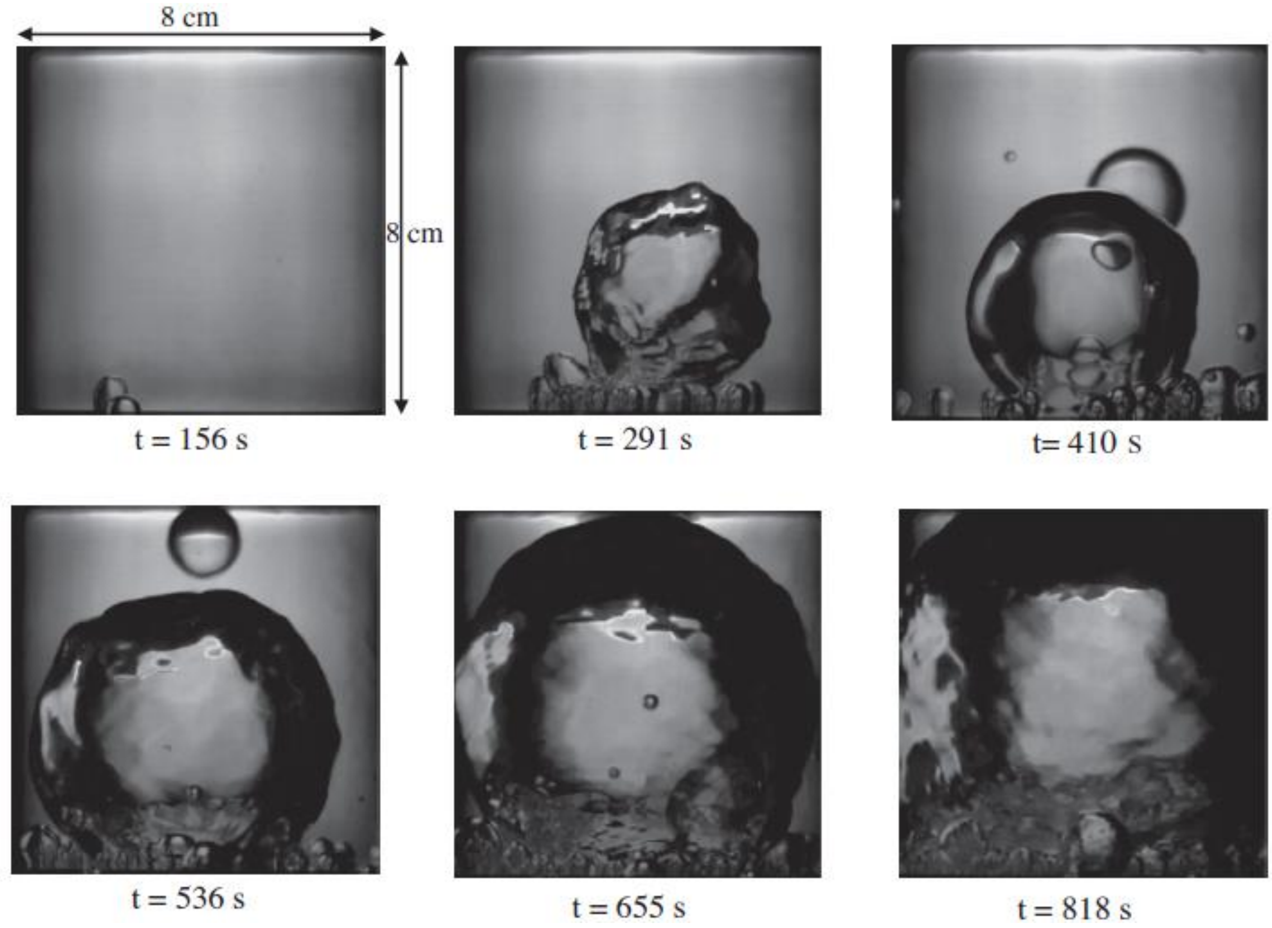

t = 156 s t = 291 s t= 410 s

t = 536 s t = 655 s t = 818 s

Figure 13: Sequences of images showing bubble nucleation and growth on the surface of the heater with smaller bubble coalescing to form one large, central bubble

As a preliminary step in overcoming this challenge, the current research group observed vapor bubble dynamics of the ratcheted microstructure in microgravity conditions. Thiagarajan et al. [27] conducted microgravity experiments in a parabolic flight with the ratcheted micro structure in a pool filled with the dielectric fluid FC-72. The test section comprised of 80 sawtooth structures with a 1 mm pitch. The asymmetric sawtooth structure was designed as a 30-60-90-degree profile with trapezoidal re-entrant cavities etched on the long slope of the structures. The complete experimental setup for the parabolic flight experiments is shown in Figure 14.

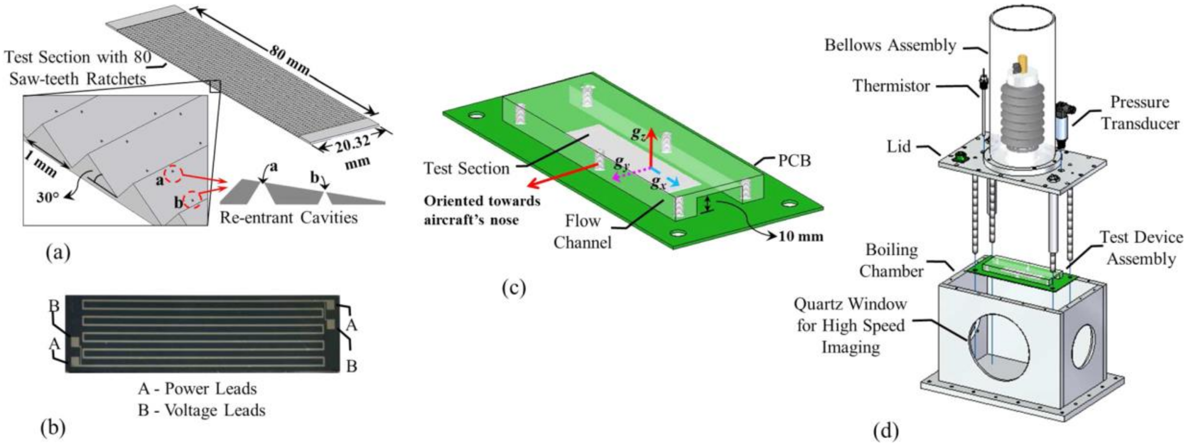

Figure 14: Complete experimental setup used in the parabolic flight experiments – Thiagarajan et al. [27]

Vapor bubbles were observed moving laterally across the microstructure at speeds as high as 27.4 mm/s. Bubble diameters were also reported to be six times larger than terrestrial experiments. Bubble dynamics differed based on the input heat flux. At a low heat flux of 0.5 W/cm^2, a smooth bubble interface was observed with no departure. At an increased heat flux of 1.4 W/cm^2, the interface was corrugated with the bubble shape appearing more spherical. The wrinkly nature of the interface was attributed to coalescence. Bubbles were also observed to depart and hover above the surface, due to momentum resulting from the coalescence process. Figure 15(a) and (b) illustrate the low and high heat flux conditions, respectively. The parabolic flight experiment was an important preliminary step in validating bubble motion along the microstructure when buoyancy forces do not significantly impact bubble dynamics.

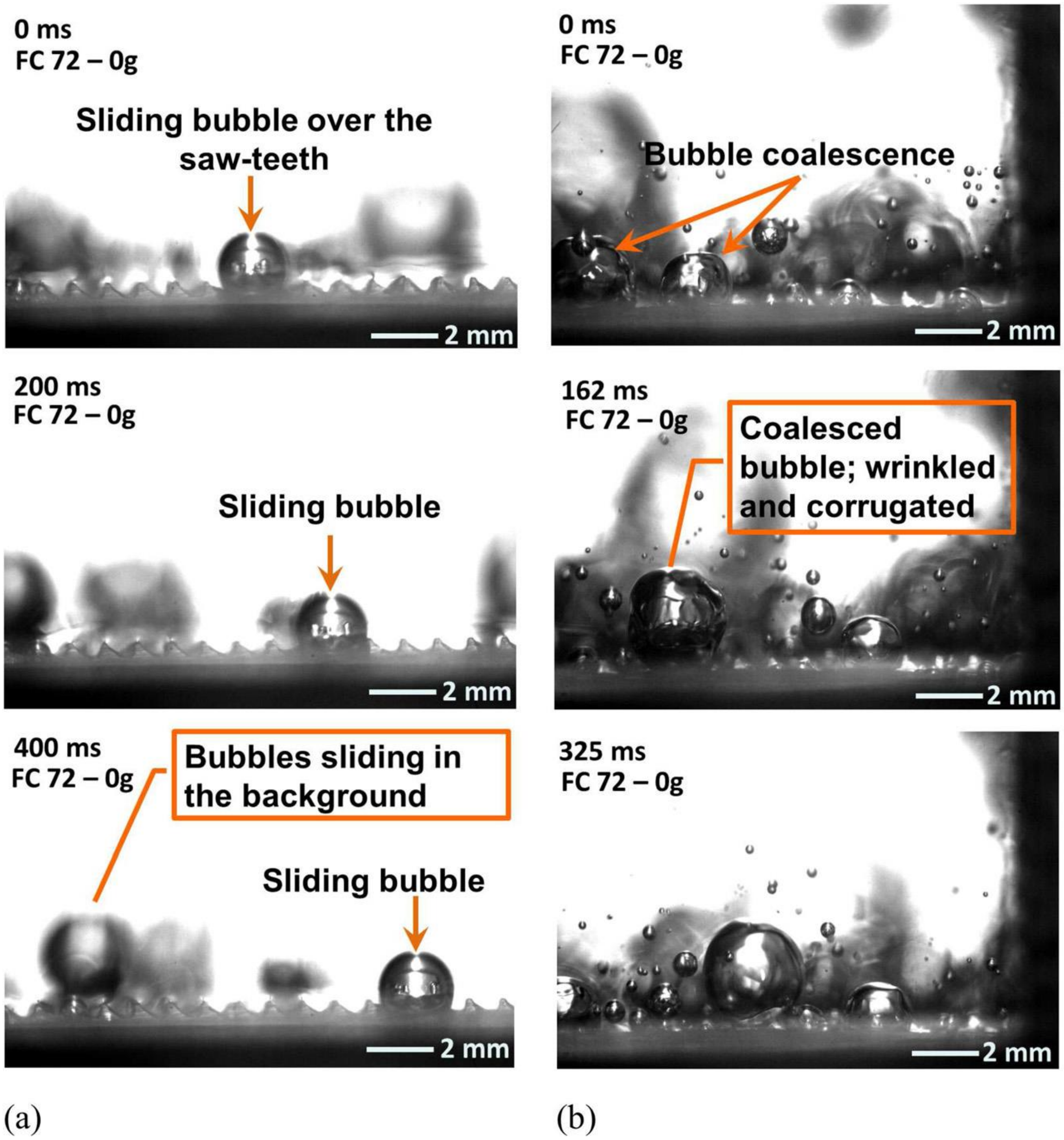

Figure 15: Bubble dynamics in FC-72 along the sawtooth microstructure under microgravity at a) q=0.5 W/cm^2 b) q= 1.4 W/cm^2

1.4 Objective of this study

The present study aims to solve the problem of stationary vapor bubbles preventing quenching fluid to rewet the surface by a ratcheted microstructure constructed of asymmetric saw teeth with square-shaped nucleation cavities. The difference in radius of curvature between the peak and valley of the asymmetric saw-tooth produces a pressure differential which acts in tandem with the imbalance to impart passive, lateral bubble motion. The resulting bubble motion is a prospective technique to slide vapor across electronic heat sources in microgravity when the diminished buoyancy forces are ineffective at detaching vapor bubbles. Preliminary NASA Zero-G flight experiments[27] have demonstrated the viability of the passive bubble motion concept, prior to an extensive study to be performed on the International Space Station under pristine microgravity conditions.

This terrestrial study is the initial phase in a larger effort to provide passive vapor bubble motion, culminating in an extensive study aboard the International Space Station (ISS) under prolonged microgravity conditions. The passive vapor bubble mobility is targeted in a confined volume of dielectric liquid in the study. The stainless steel surfaces used in the study were fabricated using an additive manufacturing technique called Powder Bed Fusion. Vapor bubble dynamics were studied across two orientations, upward-facing and downward-facing, along with high-speed imagery. The downward-facing orientation explored in this terrestrial study is the bridge between the terrestrial and microgravity experiments, as buoyancy forces do not detach vapor bubbles from the surface. The asymmetric sawtooth microstructure influenced bubble dynamics in both orientations, with vapor bubbles sliding across the microstructure in the downward-facing orientation, as shown in Figure 16. Distinct stages of bubble growth and motion, including nucleation, coalescence and sliding of the vapor bubble, were observed in the downward-facing configuration. A thin non-uniform liquid film, hypothesised to be an important factor in inducing motion, was explored using high-speed imagery. The discussed microstructure is a passive, pump-less and self-regulating cooling solution for electronics in microgravity and spacecraft applications.

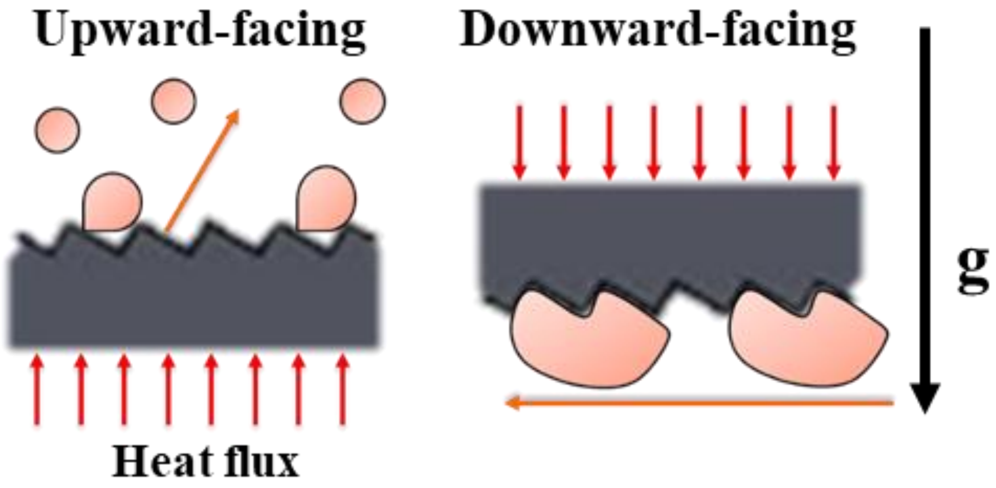

Figure 16: Schematic showing vapor mobility effected by the sawtooth microstructure in both upward-facing (left) and downward-facing (right) orientations.

CHAPTER 2 EXPERIMENTAL SETUP

This section outlines the hardware, equipment, and design protocol requirements for the terrestrial investigation (pre-cursor to ISS microgravity experiments) at Auburn University's Enhanced Heat Transfer Laboratory. Details of test surface geometry, borosilicate glass ampoule design and complete test facility assembly is discussed. Auxiliary steps such as post-processing of test surfaces is also described in this section

2.1 Test surface geometry:

The test surface consists of mirroring ratcheted sections separated by a central, unheated, flat section of 20 mm in length. The sawtooth structures have a pitch of 1 mm and consist of two variations – 60°-30° structure or 75°-15° structure, as shown in Figure 17. Other details of the test surface parameters are provided in Table 3 and illustrated in Figure 18.

The test surfaces were fabricated using powder bed fusion, a metal additive manufacturing technique and were electropolished after heat treatment to obtain a smooth surface. Powder bed fusion for metals is accomplished by fusing layers of metal powder additively to fabricate a part. After a layer of metal powder is deposited, a laser delivery system, supported by a scanner, focuses the laser beam onto a spot. The above process is repeated for all points on the build platform to complete a layer. An inert gas, like nitrogen or argon, is passed over the bed to prevent oxidation and clear any residual spatter from the previous layer [28]. The fabrication steps are repeated layer-by-layer to complete a part. The additive manufacturing process is illustrated in Figure 19. Complex geometry, like a ratcheted microstructure with embedded cavities, can be manufactured using the laser powder bed fusion process. A variety of metals and their alloys can be fabricated by controlling the process parameters like layer thickness, spot size, powder bed temperature, laser power and scanning speed.

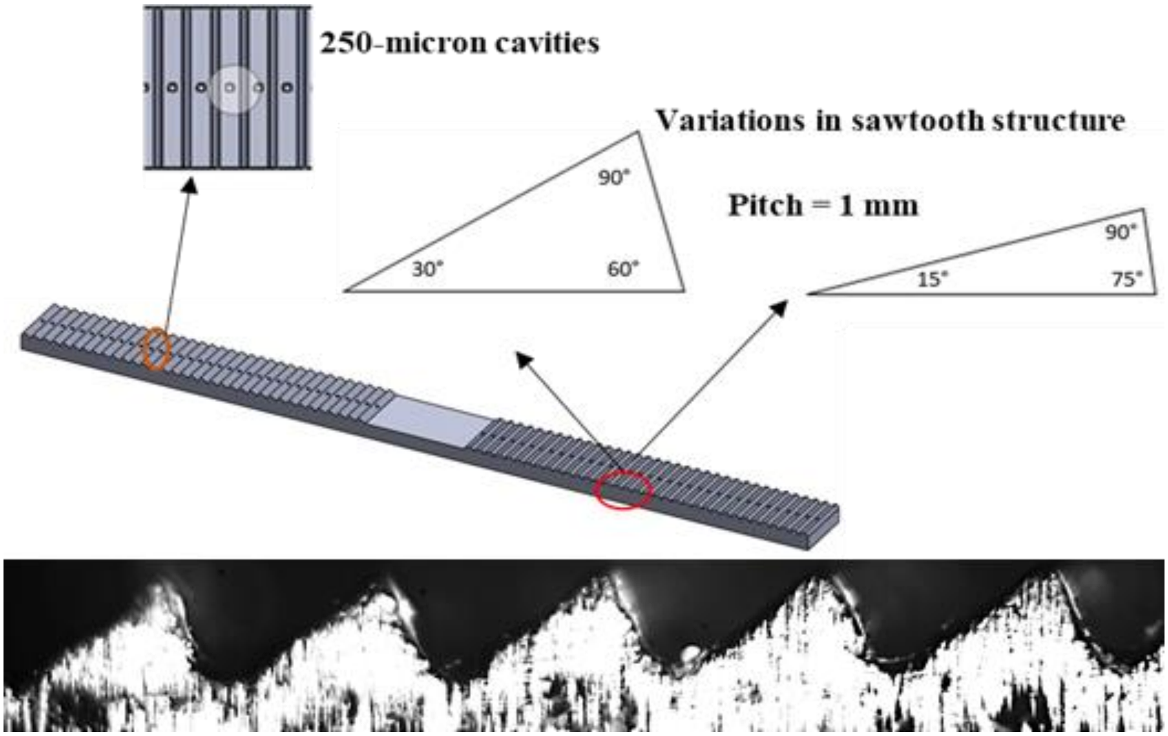

Figure 17: Details of additively manufactured test surfaces with differing sawtooth structures and 250 μm cavities (top). High-speed frame showing the microstructure in focus (bottom)

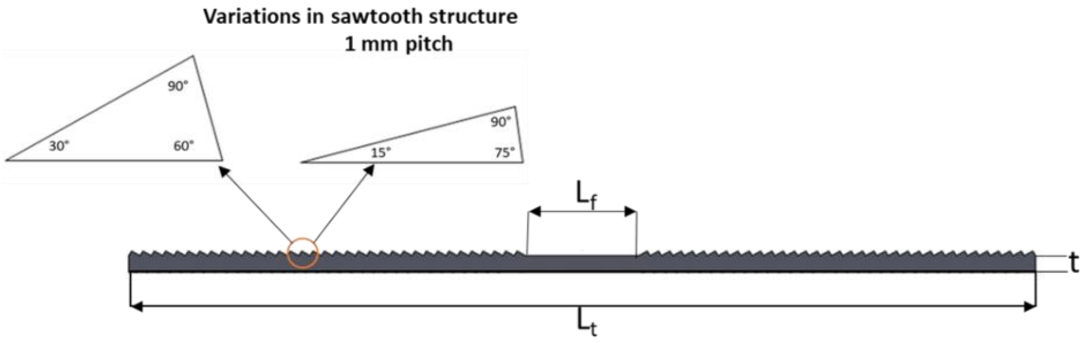

Figure 18: Illustration of test surface parameters from Table 3

Table 3: Parametric variations of test surface dimensions explored in the study

Test surface parameter	Variations
Sawtooth structure	60°-30° or 75°-15°
Heated length	50 mm (one side) or 100 mm (both sides)
Height of test surface (t)	2 mm (fixed)
Width of test surface	6 mm (fixed)
Nucleation site density	1-mm or 2-mm apart
Test surface metal	SS 316L or Ti6Al4V
Unheated central length (L_f)	20 mm (fixed)
Total length (L_t)	120 mm or 180 mm

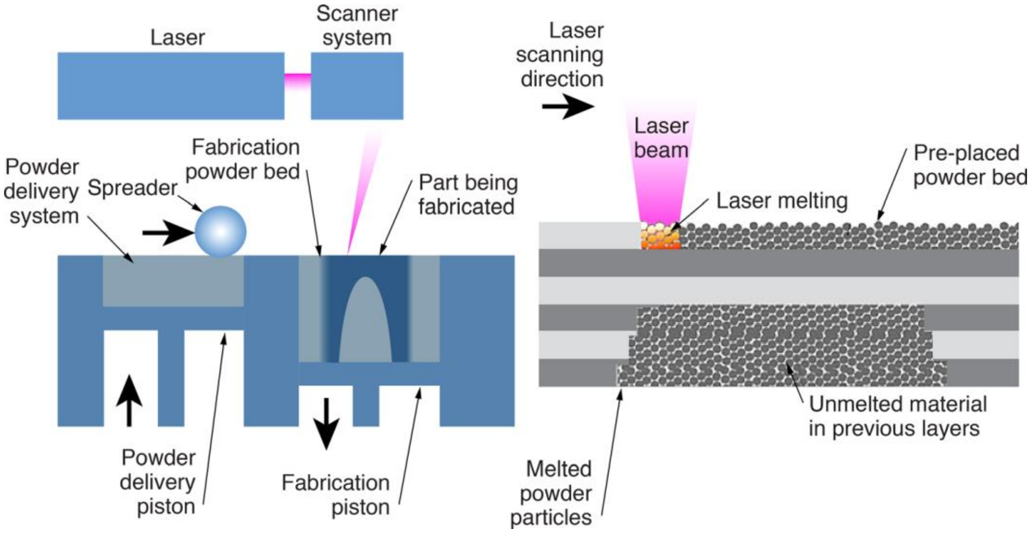

Figure 19: Illustration of the laser powder bed fusion process [28]**.**

The stainless steel surfaces used in this study were electropolished in-house to obtain a smooth surface and mirror finish. The electrolyte comprised of 25% wt. sulphuric acid and 75% wt. phosphoric acid while the cathode was a flat piece of stainless steel. The test surface to be polished was connected as the anode before being immersed into the solution. The titanium alloy was chosen as a variation due to its close coefficient of thermal expansion match with borosilicate glass. The titanium surface used in this study was electropolished using a third-party vendor, as in-house electropolishing carried safety hazards.

The differences in cavity density is illustrated in Figure 20.

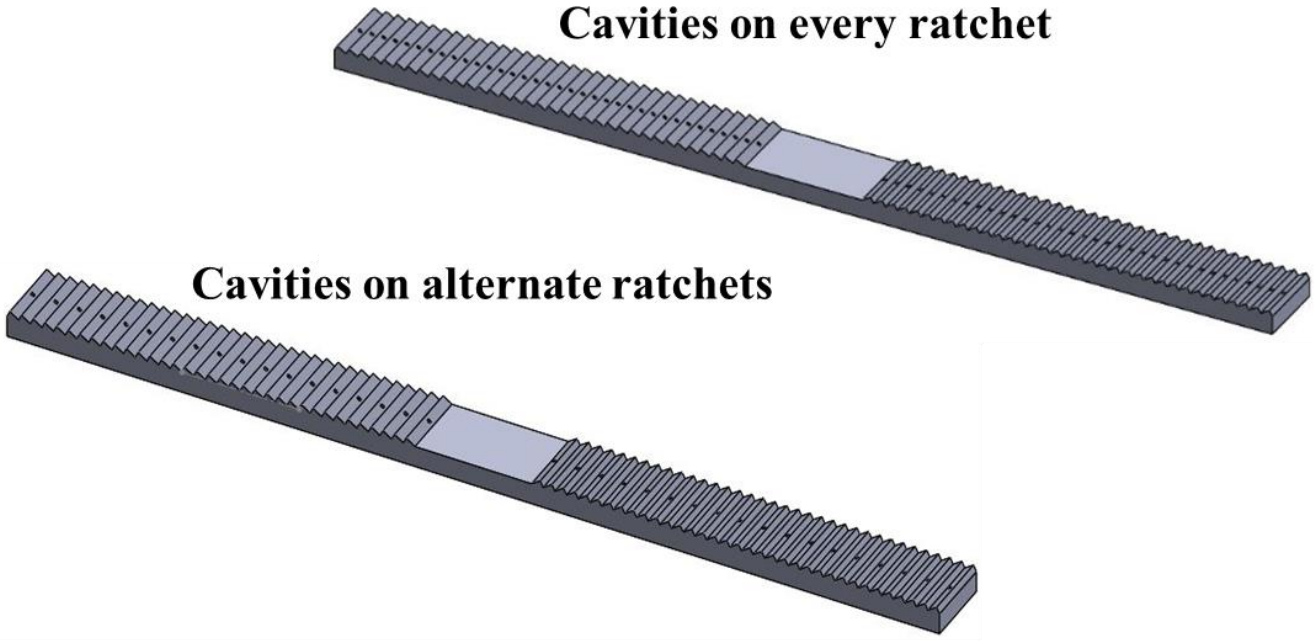

Figure 20: Visual comparison of a variation in test surfaces by varying nucleation site density

The complete test surface matrix is listed in Table 4.

Table 4: Parametric variation of test sections

Sawtooth Structure	**Cavity Density**	**Total Length of Test Surface**
30°, 60°, 90°	All	120 mm
30°, 60°, 90°	Alternate	120 mm
15°, 75°, 90°	All	120 mm
15°, 75°, 90°	Alternate	120 mm
30°, 60°, 90°	All	180 mm
30°, 60°, 90°	Alternate	180 mm

In addition to the ratcheted test sections, two baseline specimens with 250 μm cavities spaced 1 mm and 2 mm apart were be fabricated with a completely flat surface to verify passive bubble motion due to the microstructure as shown in Figure 21.

Top view of baseline specimen

Figure 21: Baseline specimen with no ratchets to verify bubble motion due to ratcheted microstructure

2.1.1 Electropolishing

After the specimens are printed using the direct laser deposition (DLD) method, they must be heat treated to remove internal stresses. This causes a small layer of rust and a rough surface finish, causing potential unwanted nucleation sites along the sharp ridge peaks of the ratchet structure.

Electropolishing is a method that takes off microscopic layers of material by passing an electrical current through the specimen while placed in an electrolyte solution. This method is the opposite of electroplating, where the workpiece is the anode. The process removes workpiece material much faster at microscopic peaks rather than valleys, smoothing out the surface and removing rust. The apparatus used involves holding the specimen with an alligator clamp at one end, placing it into n phosphoric acid and sulphuric acid electrolyte, and manually stirring the solution. A voltage of 20 V is passed through the setup for 20 minutes to obtain the desired finish.

The process ensures a smooth surface finish and significant reduction of extraneous nucleation sites on the test section. The roughness of the test surface was measured using a surface profilometer with a contacting stylus tip. For a representative stainless steel surface, the RMS (root mean squared) roughness measured after the additive manufacturing process with the heat treatment was 28.2 µm. After electropolishing the test surface for 20 minutes, the RMS roughness was reduced to 12.2 µm.

2.2 Ampoule Design:

The Pore Formation and Mobility During Controlled Directional Solidification in a Microgravity Environment Investigation (PFMI) furnace available for ISS experiments (shown in Figure 21, top) currently can house a borosilicate glass ampoule with an outer diameter of 12 cm and a length of 30 cm to conduct experiments (shown in Figure 22, bottom). As this terrestrial experimental setup was created to closely align with the available dimensions of PFMI furnace, several features were fabricated using a combination of glass blowing techniques and metal-to-glass transitions. As the microstructure requires a flat surface, the 12 mm circular profile was converted into a square borosilicate glass tube with 8 mm I.D and 1.2 mm wall thickness with two square-circular transitions on either end for inlet or access ports. Two strategically located ports were added on the top face of the ampoule to facilitate positioning and adhering the specimen in the center of the glass tube. A T-shaped junction was created at the side face of the glass tube with two distinct pathways -the vertical path leads to the bellows where the effects of vapor expansion are mitigated, and the horizontal pathway leads to the data collection system. An end-located access port with a circular profile of 10 mm ID was used as a pathway for the k-type thermocouples. This design serves to mimic the final desired version of the ISS ampoule which will include circular transitions on both ends of the central square section to allow retrofitting into the PFMI furnace module on ISS. A stainless-steel bellows (2.375" (6.03 cm) I.D) with an empirically measured spring rate of ~26.97 N/mm was used to accommodate volume dilation due to vapor production during the experiment. The bellows is an aspect of the terrestrial experiment not expected to carry over to the ISS experiments. The complete experimental setup is shown in Figure 23.

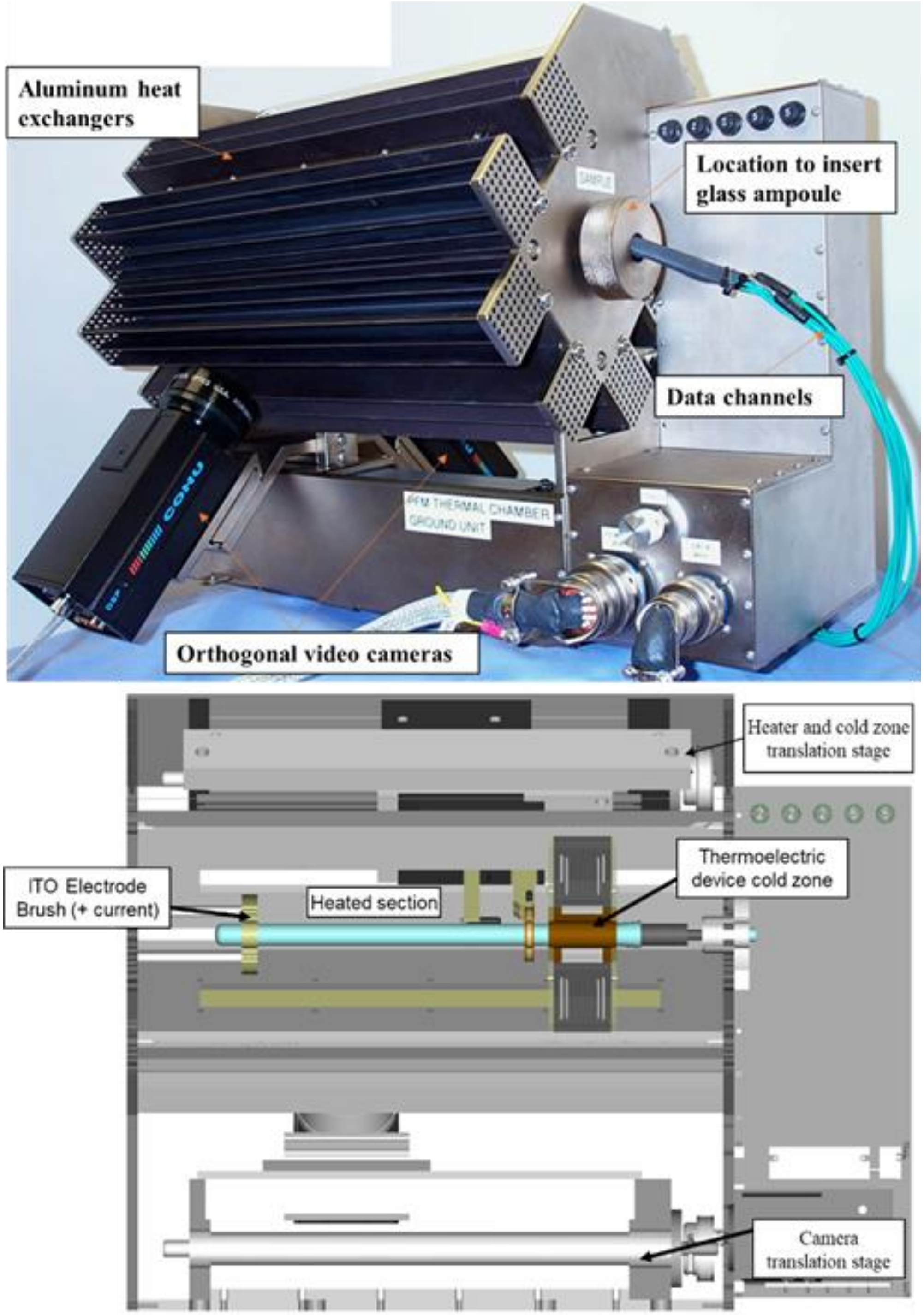

Figure 22: Feature of the PFMI furnace available for ISS experiments (top) and furnace section view (bottom)(adapted from [29])

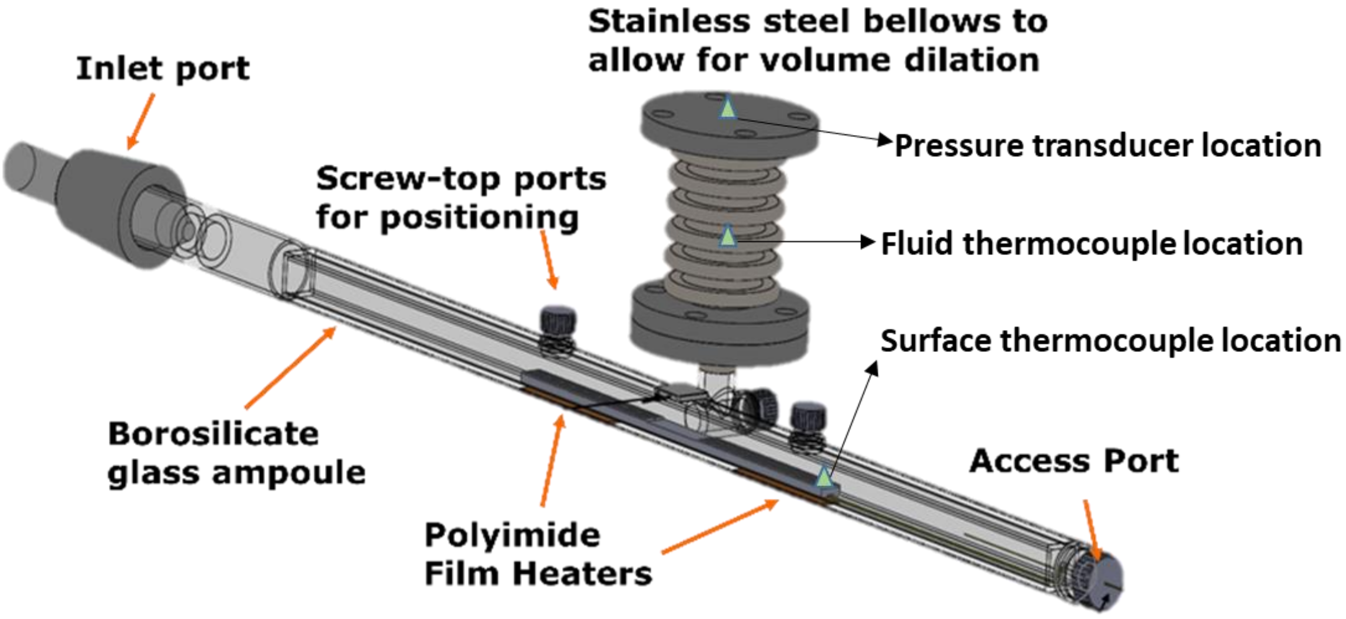

Figure 23: Isometric view of the complete ground experiment setup with positioning details of bellows and ports. The temperature and pressure measurement locations are highlighted.

The test surface was adhered to the glass using Arctic Silver thermal epoxy. Polyimide film heaters were mounted to the glass using Kapton™ adhesive and insulated using expanded polystyrene to ensure negligible heat loss. To mimic the thermoelectric device zone (TED) in the PFMI furnace (shown in Figure 22, bottom), a few experimental runs were conducted using a regulated waterblock placed in the center of the borosilicate glass tube. However, test surface variations reported in the current study such as sawtooth structure, nucleation site density and heated length were studied without use of the waterblock.

A Phantom™ v310 high-speed camera outfitted with an Infinity microscope lens attachment was used to enable high-speed imaging. The dielectric liquid was degassed prior to experimental runs in the setup using a rope heater (Briskheat™ model HSTAT101006) wrapped around the bellows and a Graham condenser to ensure removal of non-condensable gases. A vacuum pump (Welch-Ilmvac™ Dryfast Ultra 2042) was connected to the inlet port and the dielectric liquid was charged using a modified flask to ensure minimal entrainment of non-condensables into the setup. Prior to a run, the tube was checked to be level for both orientations using a digital angle gauge calibrated to ± 0.1° by measurement at two locations on the horizontal, square section.

LabVIEW™ was used to measure all temperature data through interfacing with a data acquisition system. Two Omega™ K-type thermocouples were used to measure temperature data at the surface, and the bulk liquid housed in the bellows. The thermocouples were calibrated against a NIST-traceable thermistor to provide a ±0.2 K temperature data uncertainty. The pressure in the closed system was measured at the top of the bellows with a pressure transducer (Omegadyne™ model no. PX319-050A5V) capable of measuring up to 50 psi. The complete experimental setup was housed in a structure mounted on pneumatic vibration isolating feet (Newport™ SLM-1A) to reduce the effect of environmental noise such as equipment vibrations on vapor mobility dynamics. The list of materials for each component is listed in Table 5.

2.2.1 Safety test of ampoule:

A preliminary borosilicate glass ampoule was tested up to a pressure of 60 psi (safety factor of 4) and a temperature of 140°C (the maximum possible temperature attainable in the PFMI module currently). These values are much higher than anything anticipated during the ISS experiments and demonstrate the reliability of the ampoule.

Table 5: List of materials for the components used in the terrestrial experiment

COMPONENT	***MATERIAL***
Test Sections	Ti-6Al-4V and stainless steel
Ampoule	Borosilicate glass
Bellows	Stainless steel
Inlet Valve	Teflon
Top Ports	Plastic caps
Drain/Access Port	Plastic caps
Heat source	All-Polyimide Film Heaters
Thermal interface to mount test section	Arctic Silver adhesive paste (99.9% pure micronized silver)
Thermal interface to mount heat source	Double-sided Kapton tape

CHAPTER 3 EXPERIMENTAL RESULTS AND DISCUSSION

The data reported in this section were collected in boiling experiments conducted using FC-72 with a subcooling of 20 K. The saturation temperature for each input heat flux was calculated based on the measured pressure of the closed system. The primary parameters for the experimental study include test surface orientation (upward-facing vs downward-facing), effect of nucleation site density (1-mm apart vs 2-mm apart), effect of test surface material (Ti-6Al-4V vs SS-316L), effect of sawtooth structure (60°-30° vs 75°-15°) and effect of heated length as shown in Table 6. Vapor bubble dynamics on baseline (flat) test surfaces were also observed to validate the effects of the sawtooth microstructure. The downward-facing configuration, an adverse situation**,** discussed in this study is the authors' attempt to bridge the terrestrial and microgravity experiments, by ensuring that vapor bubbles are not lifted off the surface due to buoyancy forces. The results of the test surfaces presented in this section were repeated at least twice for repeatability purposes. To reduce data redundancy and promote clarity of presented data, representative data are shown in each section below. A sample repeatability plot is shown in Figure 24.

Table 6: The range of parameters explored in the experimental study

P**arameter**	R**ange/Description**
Test surface orientation	Upward-facing, Downward-facing
Nucleation site density	1-mm apart, 2-mm apart
Test surface material	SS-316L, Ti-6Al-4V
Sawtooth structure	60°-30° vs 75°-15°
Effect of heated length	50 mm vs 100 mm (downward-facing surface only)

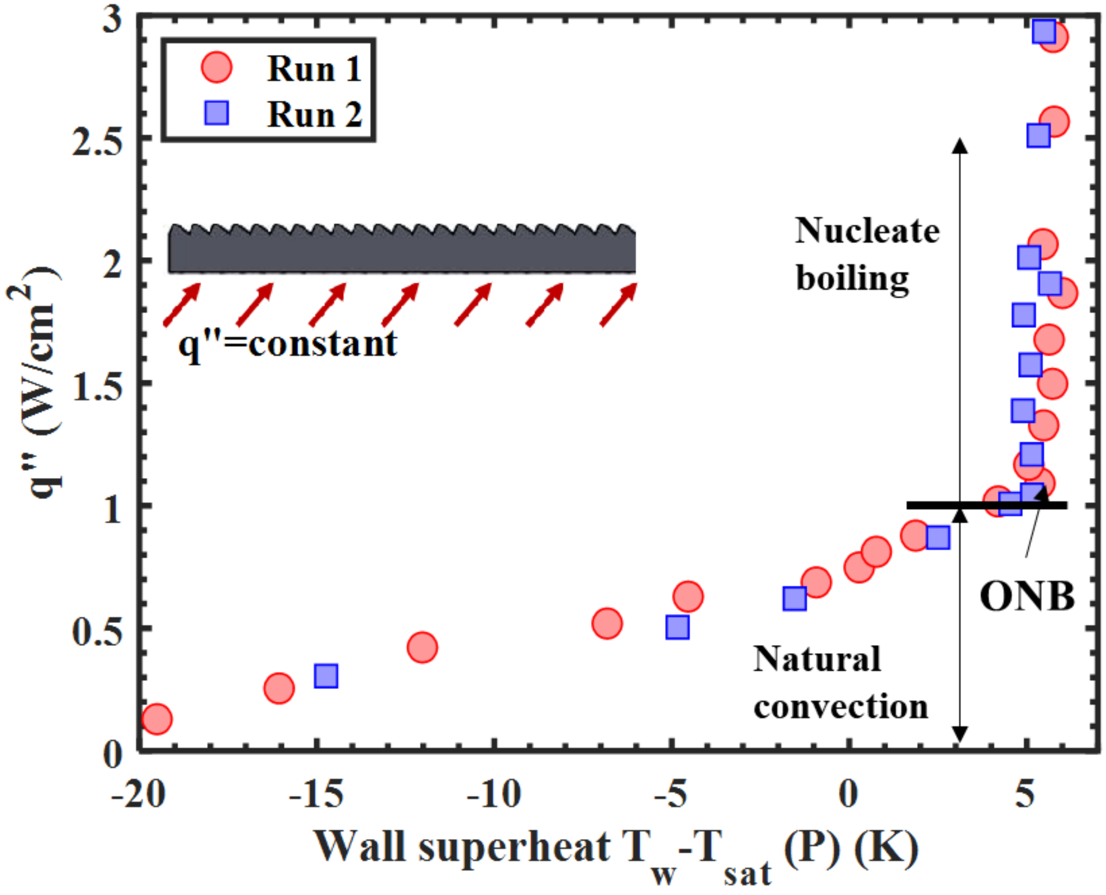

Figure 24: Repeatability plot for an upward-facing 60°-30° sawtooth test surface with cavities spaced 1-mm apart

The x-axis indicates the wall superheat, which is calculated as the difference between the wall temperature and saturation temperature (calculated at the pressure measured in the closed system). The y-axis displays the input heat flux, calculated as the input heat flux divided by the total heated area. The image on the top-left of the figure indicates the orientation in which the test surface is heated along with the wall conditions (constant heat flux). Nucleation was observed in most cavities at heat fluxes as low as 1 W/cm^2, signifying the onset of nucleate boiling (ONB). At successive higher heat fluxes, the rise in wall superheat is much more gradual compared to lower heat fluxes. This is indicative of different heat transfer regimes – natural convection at lower heat fluxes and nucleate pool boiling at heat fluxes > 1 W/cm^2 (as verified by high-speed imagery).

3.1 Geometry effects

In a typical pool boiling scenario, a large "pool" of liquid is available to clearly distinguish the different boiling regimes and study the effects of a surface microstructure in detail. However, in the present study, the available liquid inventory within the tube is low enough to significantly alter boiling behavior – primarily due to vapor production. Combined with the fact that the microstructure induces flow in the downward facing configuration through vapor mobility, the lines between pool boiling and flow boiling are blurred. Due to the complex effects in play here, the results presented below cannot be interpreted within the limits of a conventional pool boiling setup.

As the heat flux nears the onset of nucleate boiling (ONB), the dielectric liquid (FC-72) starts creating vapor. Vapor starts travelling to the bellows to condense, and a liquid-vapor interface forms in the tube. With increasing heat flux, more vapor is created, eventually leading to dryout as shown in Figure 25. For the downward facing orientation, the effects of vapor production are more acute due to proximity to the liquid-vapor interface. The lower liquid inventory afforded to the liquid-vapor interface, combined with vapor production over the surface leads to dryout at low heat fluxes. Therefore, the dryout conditions for both orientations are not a limit of the liquid properties or microstructure but directly related to the low inventory afforded by the tube's confined cross section.

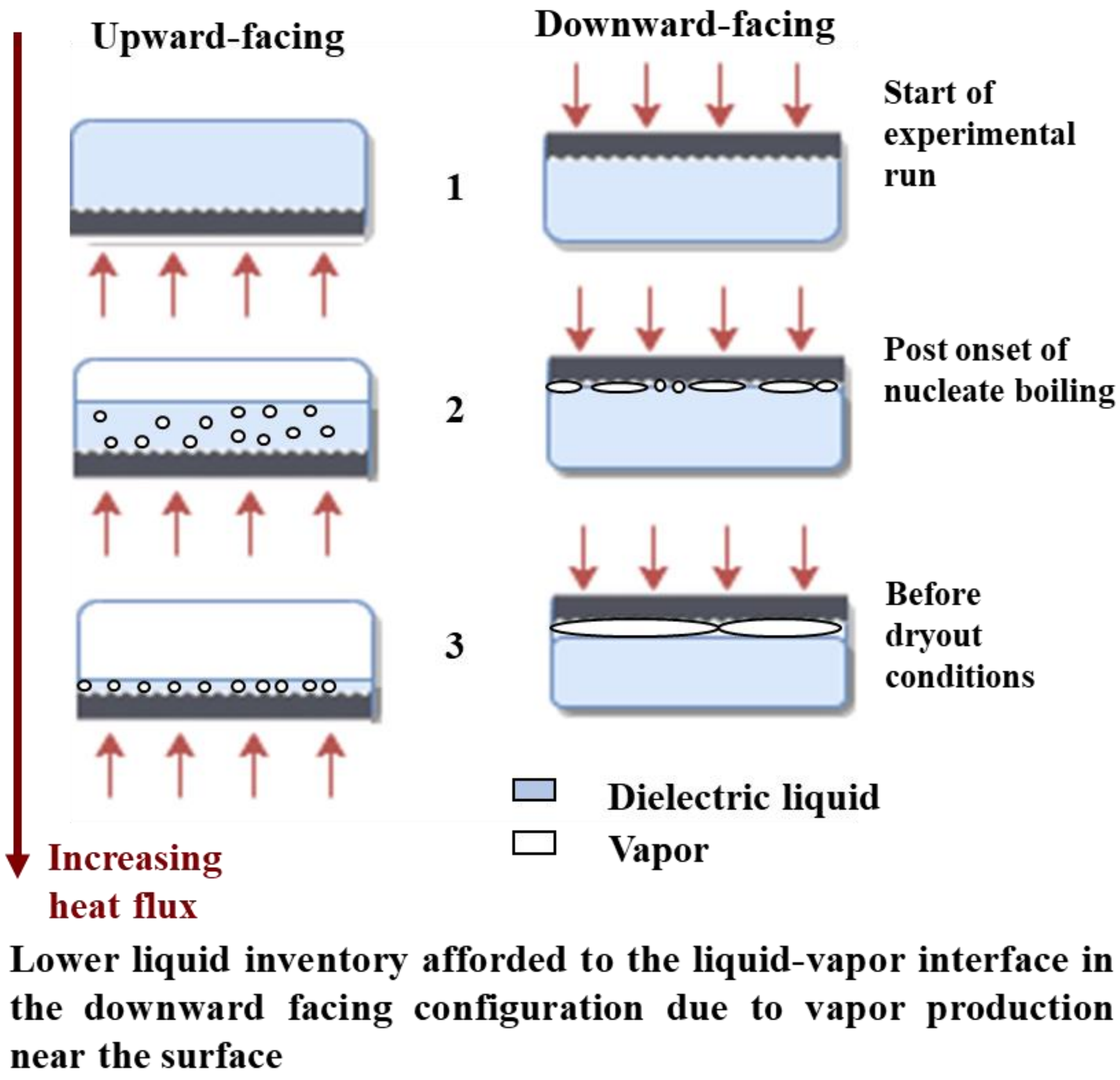

Figure 25: Schematic showing side-view of the cross-section of the square tube to demonstrate vapor production in the closed system at three stages during the experimental runs for both upward-facing and downward-facing orientations

3.2 Effect of surface orientation (upward-facing vs downward-facing)

As expected, the effect of surface orientation significantly altered boiling behavior as shown in Figure 26. For the downward-facing surface, nucleation is observed at heat fluxes as low as 0.88 W/cm^2 compared to 1.1 W/cm^2 for the upward facing surface. It is also seen that dryout is observed at 2.5 W/cm^2 for the downward facing surface, while similar dryout conditions were observed for the upward-facing orientation at ~3 W/cm^2. This limit is not attributed to the microstructure's efficacy in moving vapor but to the small, square cross section of the ampoule, which limits the amount of available liquid inventory. Though there is a clear pathway to the condenser (bellows) located centrally, vapor generation is high enough within the tube at higher heat fluxes to surpass outflow to the condenser. An interesting feature of the plot is the relatively low superheat required for onset of nucleate boiling (ONB) observed for the downward-facing surface.

3.3 Upward-facing surfaces

Bubble diameter and frequency was measured using frames extracted from the high-speed videos. The images were calibrated using known sawtooth dimension (1 mm pitch) and used to measure bubble departure diameter, departure frequency and velocity. The velocity of the departing bubbles was calculated using center of mass analysis, assuming that the vapor has uniform density throughout the bubble. The bubble was assumed to be axisymmetric about the third dimension, to apply the equivalent diameter for image processing. Image J [30] software was used for all image processing steps. At a heat flux of 1.05 W/cm^2 as described in Figure 27, the bubble departure diameter was consistently resolved between 1 and 1.12 mm with no significant decrease in diameter as the bubbles departed the surface within the frame of view. The departure frequency was observed to be between 38 and 41 Hz, with the velocity of departing bubbles maintained in the range of 71-77 mm/s. The departure diameter and velocity of departing bubbles did not change significantly within the range of input heat fluxes. The vapor bubble's nucleation and growth along a 60°-30° sawtooth is illustrated in Figure 28. To ensure that the lateral direction imparted to the vapor bubbles was not due to misalignment, the symmetric, mirrored ratcheted sections (as shown in Figure 2) were simultaneously heated. Alignment was confirmed as the vapor bubbles on the right half moved in opposite direction to the vapor bubbles on the left half, towards the tube's center.

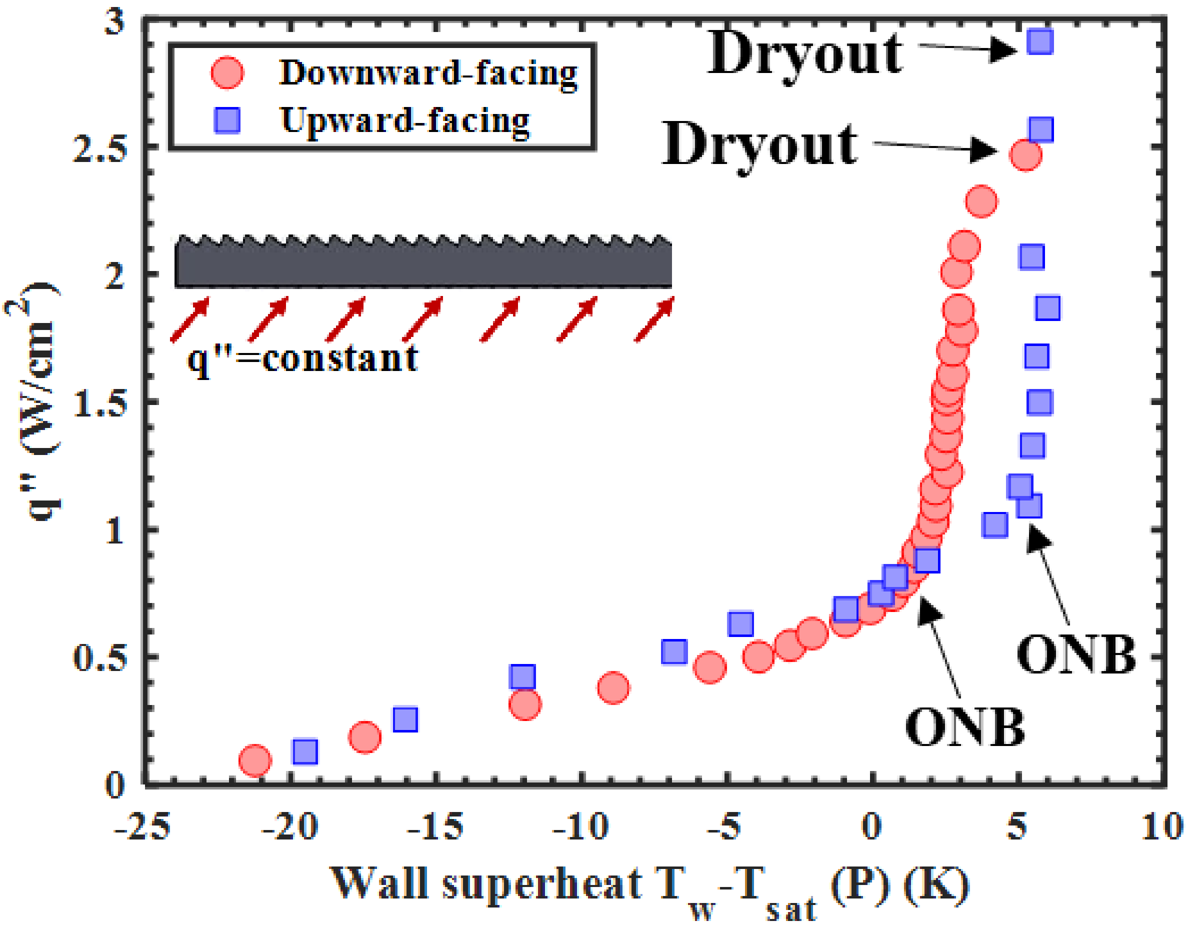

Figure 26: Wall superheat as a function of input heat flux for a 60°-30° sawtooth test surface with cavities spaced 1-mm apart

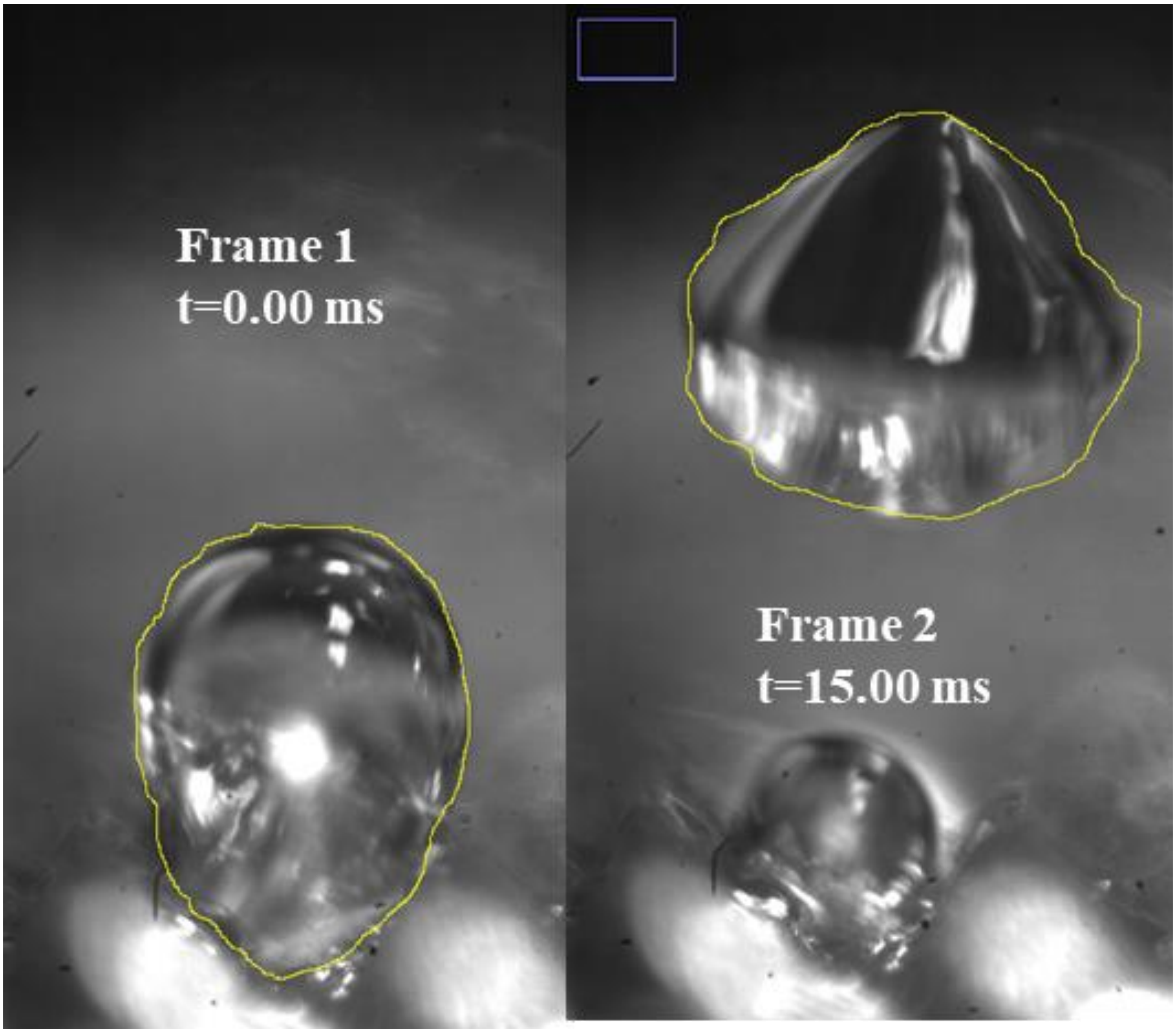

Figure 27: Sequence of images showing vapor bubble (outlined) nucleation and departure from a 250-micron cavity on 60°-30° sawtooth with the input heat flux at 1.05 W/cm^2. Due to the narrow depth of field afforded by the high-speed camera, the vapor bubbles are in sharp focus while the sawtooth features are blurred. (1280x800, 1000 fps)

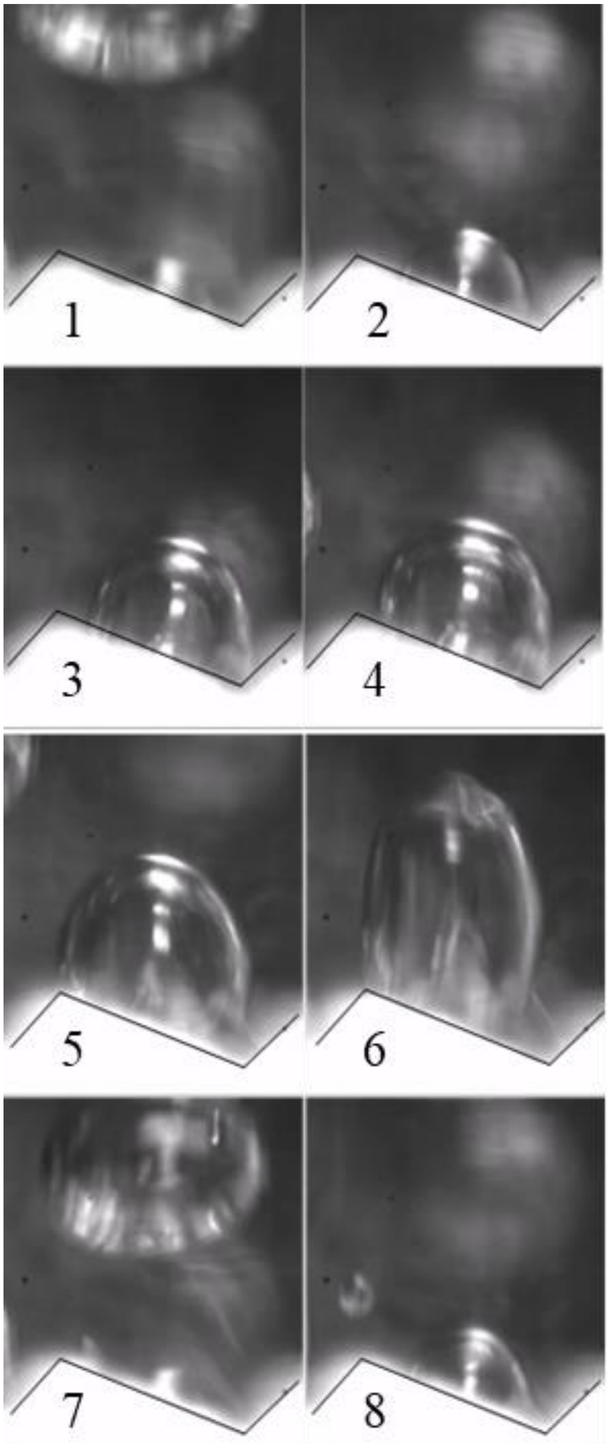

Figure 28: Series of images showing bubble nucleation and departure from a 250 µm cavity on a 60°-30° sawtooth (outlined in black) Frames 1-4 show the initial stages of bubble growth with a lateral component due to the surface microstructure. Frames 5-8 show the later stages of bubble growth and departure where the buoyancy forces dictate the departure direction. Bubble lifecycle was recorded over ~24 ms. (1280x800, 1000fps)

3.4 Downward-facing surfaces

For the downward facing surface, high-speed imaging was unclear with the 60°-30° sawtooth due to fluid perturbations. Therefore, a 75°-15° sawtooth structure was fabricated for better visualization of bubble dynamics. Flattened vapor bubbles were seen nucleating, coalescing and sliding across the surface from right to left in the nucleate boiling regime as shown in Figure 29. During nucleation incipience, multiple nucleated vapor bubbles were observed to coalesce before sliding along the microstructure. Sometimes, these coalesced bubbles would merge to form an even longer slug, which would quickly move across the microstructure in the intended (from right to left) direction. As the heat flux increased, the frequency of these slug formation events was observed to increase.

When the surface was covered by a fast-moving vapor slug, a subtle but distinct interface was seen moving along the asymmetric ratchets, as shown in Figure 30. Upon closer inspection, the liquid-vapor interface pattern was due to the vapor bubbles riding on a thin film of liquid, in line with observations by previous researchers who explored the dynamics of the asymmetric ratchet in microgravity[27]. When the Edge Sobel horizontal filter was applied to the image, the interface came into sharp focus. The liquid film was found to be non-uniform as the liquid film is thicker at the trough compared to the crest of the sawtooth. Using the calibration techniques described previously in this thesis, the liquid layer was determined at two distinct locations- the crest and trough of the sawtooth. For the 75°-15° sawtooth, this measurement of the liquid film was made possible at different heat fluxes with backlit and front lit high-speed imagery. Overall, it can be seen that the average liquid film thickness at both locations increase with increasing heat flux as shown in Table 7.

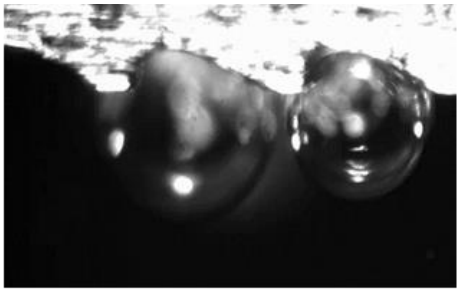

Nucleation (t=0.00ms)

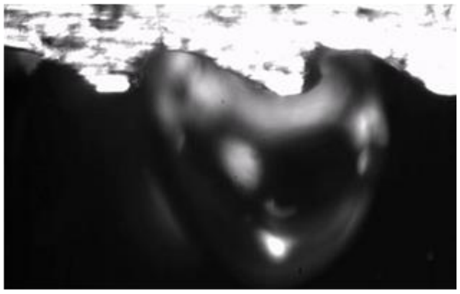

Coalescence (t=19.00ms)

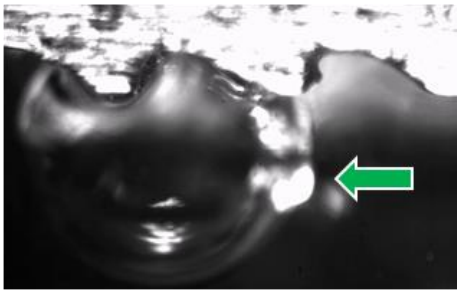

Sliding vapor bubble
(t=53.00 ms)

Figure 29: Sequence of images showing bubble nucleation, coalescence and sliding across the microstructure (from left to right) on a 75°-15° sawtooth in the downward-facing orientation (1280x800, 1000 fps)

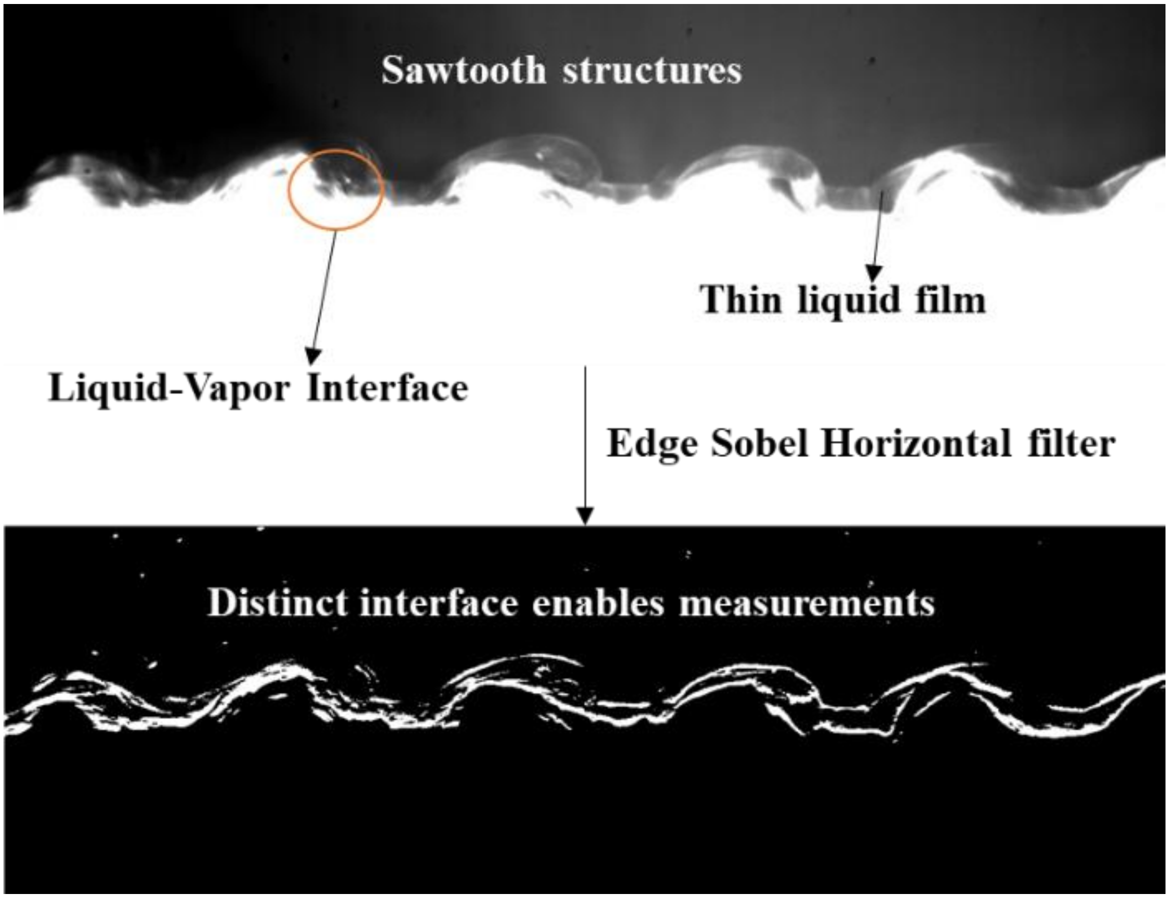

Figure 30: Liquid-vapor interface of a sliding vapor slug in FC-72 in a downward-facing orientation at 2.5 W/cm^2. When an edge filter is applied to the backlit, contrasted image, the interface comes into sharp focus to enable measurements. (1280x800, 700 fps)

Table 7: Measurements of liquid film thickness at different heat fluxes for the 75°-15° sawtooth structure

Input Heat Flux (W/cm^2)	**Average liquid film thickness at crest (µm)**	**Average liquid film thickness at trough (µm)**
1.25	46	124
1.78	74	180
2.5	113	235

Based on high-speed imagery, two distinct bubble regimes were observed for the downward-facing surface as shown in Figure 31. At low heat fluxes (0.8~1.4 W/cm^2), coalesced bubbles spread across three to four sawteeth slid along the microstructure. At higher heat fluxes (>1.4 W/cm^2), a continuous, moving vapor slug forms across the surface spanning across the frame of view.

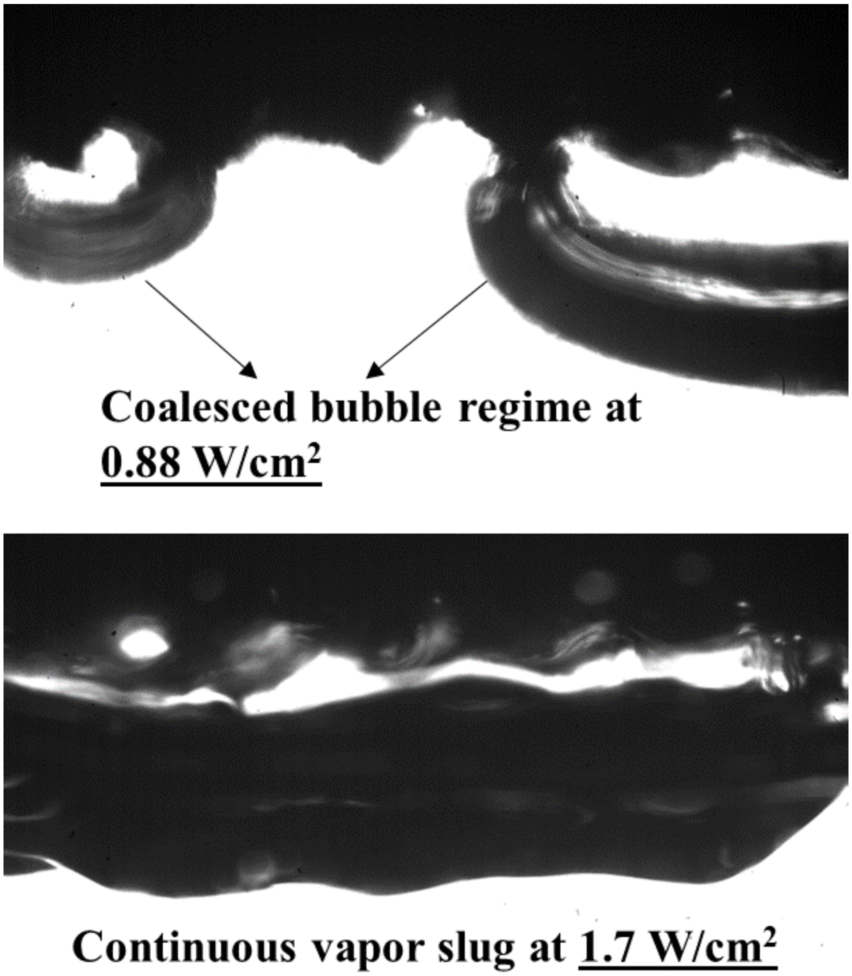

Figure 31: Vapor bubble regimes in the downward-facing configuration for 60°-30° sawtooth at two heat fluxes, 0.88 W/cm^2 (top) and 1.7 W/cm^2 (bottom) (1280x800, 2000 fps)

3.5 Cavity density for upward-facing surfaces

For the test surfaces with cavities spaced 1-mm apart, the onset of nucleate boiling was observed at a superheat close to 4.5 K lower than the test surface with cavities spaced 2-mm apart, given a constant heating length as shown in Figure 32. This result is in line with expectations and validates the role of 250 µm cavities as effective nucleation sites. Apart from significantly altering the boiling curves, the nucleation site density influenced the clarity of high-speed imaging. Vapor bubbles were easier to capture with high-speed imagery for test surfaces with cavities located 2-mm apart due to lower image distortion with the field of view as shown in Figure 33. For cavities located closer, the continuous nucleation and departure of vapor bubbles hindered clear imaging due to constant fluid motion.

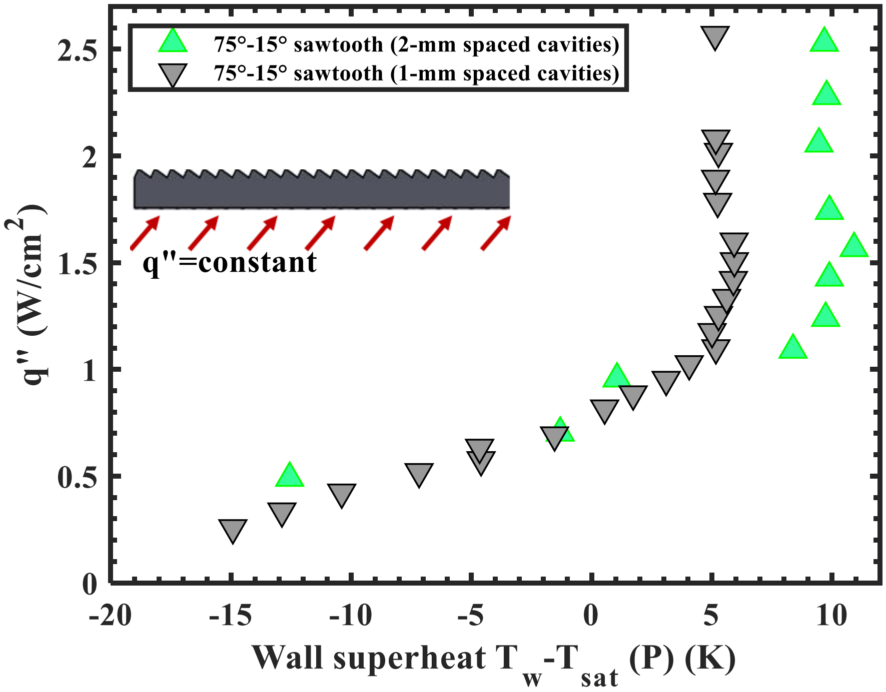

Figure 32: Effect of nucleation site density on upward-facing surfaces with a 75°-15° sawtooth structure

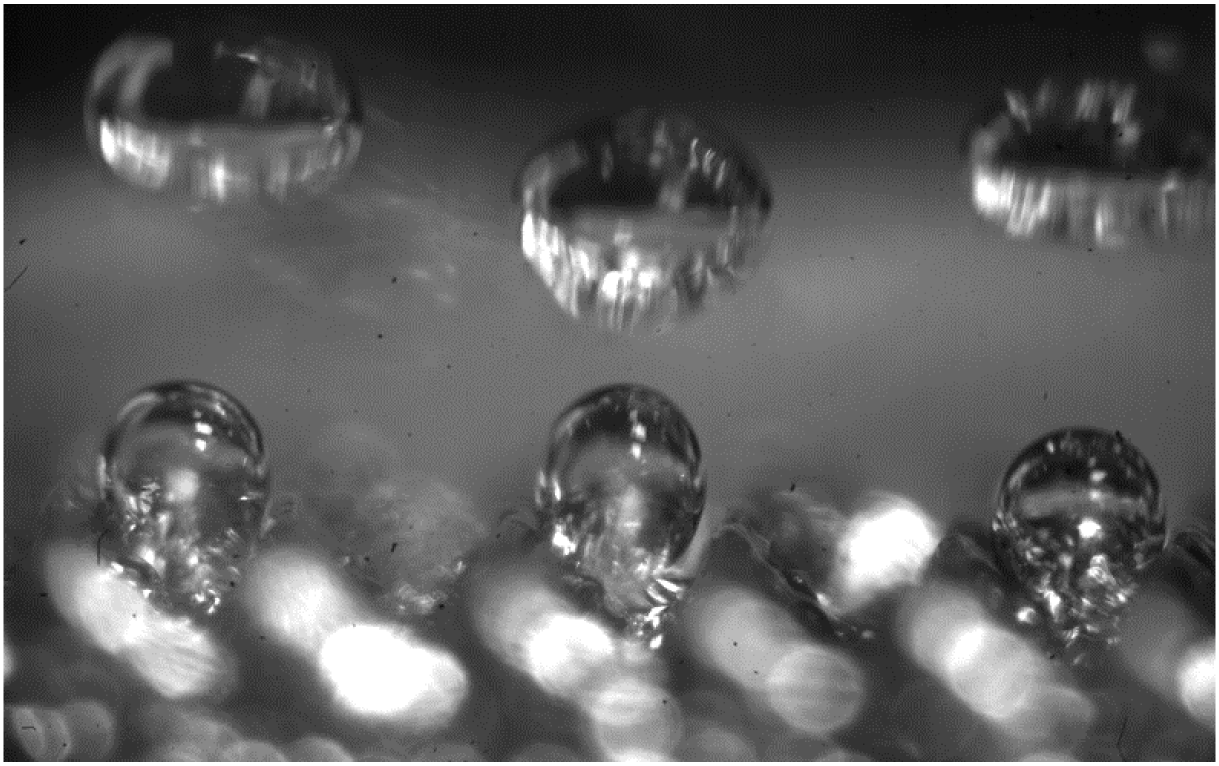

Figure 33: Bubble nucleation and departure from three 250-micron cavities on a 60°-30° sawtooth test surface with cavities spaced 2-mm apart. High-speed imaging is focused on the vapor bubbles due to low distortion from fluid motion. (1280x800, 1000fps)

3.6 Effect of test surface material for upward-facing surfaces

While the bulk of the terrestrial runs were performed with stainless steel surfaces, titanium alloy surfaces were also fabricated in preparation for the microgravity flight experiments. After a careful review of the metal alloy options available for additive manufacturing, stainless steel, and titanium alloy (Ti-6Al-4V) were selected for their close coefficient of thermal expansion (C.T.E) match to borosilicate glass. Minimal C.T.E discrepancy between the glass and the test surface lowers the thermal stresses developed in the interface during the experiment. The C.T.E values for the borosilicate glass and metal surfaces have been detailed in Table 8. Test sections fabricated from stainless steel have a higher CTE mismatch to the borosilicate glass ampoule and subsequently lead to higher stresses.

Table 8: Coefficient of thermal expansion values for borosilicate glass and metal test surfaces

MATERIAL	***C.T.E. (K^{-1})***
Borosilicate Glass	3.3×10^{-6}
Ti6Al4V (Titanium alloy)	$8 \times 10^{-6} – 9 \times 10^{-6}$
Stainless Steel 316 L	16×10^{-6}

The family of additively fabricated Ti-6Al-4V surfaces are shown on the baseplate in Figure 34. The surfaces were then heat treated at 735°C for stress relief and air cooled to ensure good overall properties[31]. Though the heat treatment was performed in an inert gas environment, thick oxide layers were formed on the test surfaces due to the air-cooling procedure. While the stainless steel surfaces were electropolished in-house to achieve smooth surface roughness, the titanium alloy surfaces were electropolished using a third-party vendor to ensure a desirable surface. The titanium surfaces were not electropolished in-house due to safety hazards of the procedure.

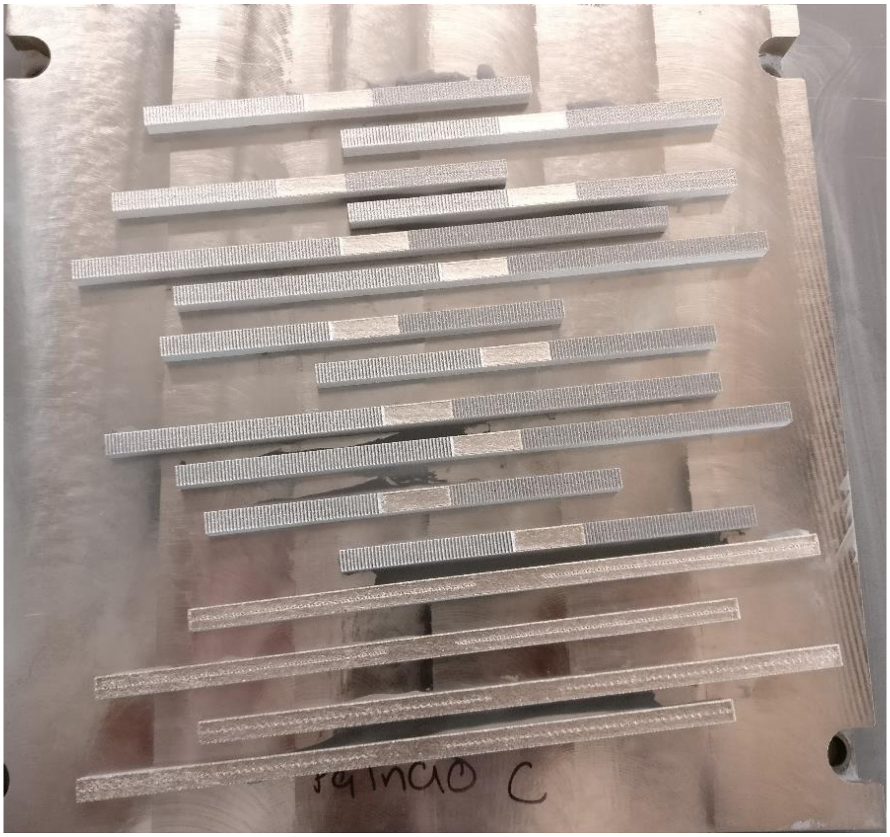

Figure 34: Additively manufactured Ti6Al4V surfaces on the baseplate

Slight differences in the boiling curve due to test surface material were observed because of varying surface preparation methods. As a result, the surface roughness and finish of the test surfaces varied. The electropolishing process for the titanium alloy surfaces did not yield a mirror finish, and as such a higher number of stray nucleation sites were expected. This led to onset of nucleate boiling at a lower superheat compared to the stainless steel surface, as shown in the figure below. The onset of nucleate boiling for the Ti6Al4V surface, however, occurs at a slightly higher heat flux (1.3 W/cm^2).

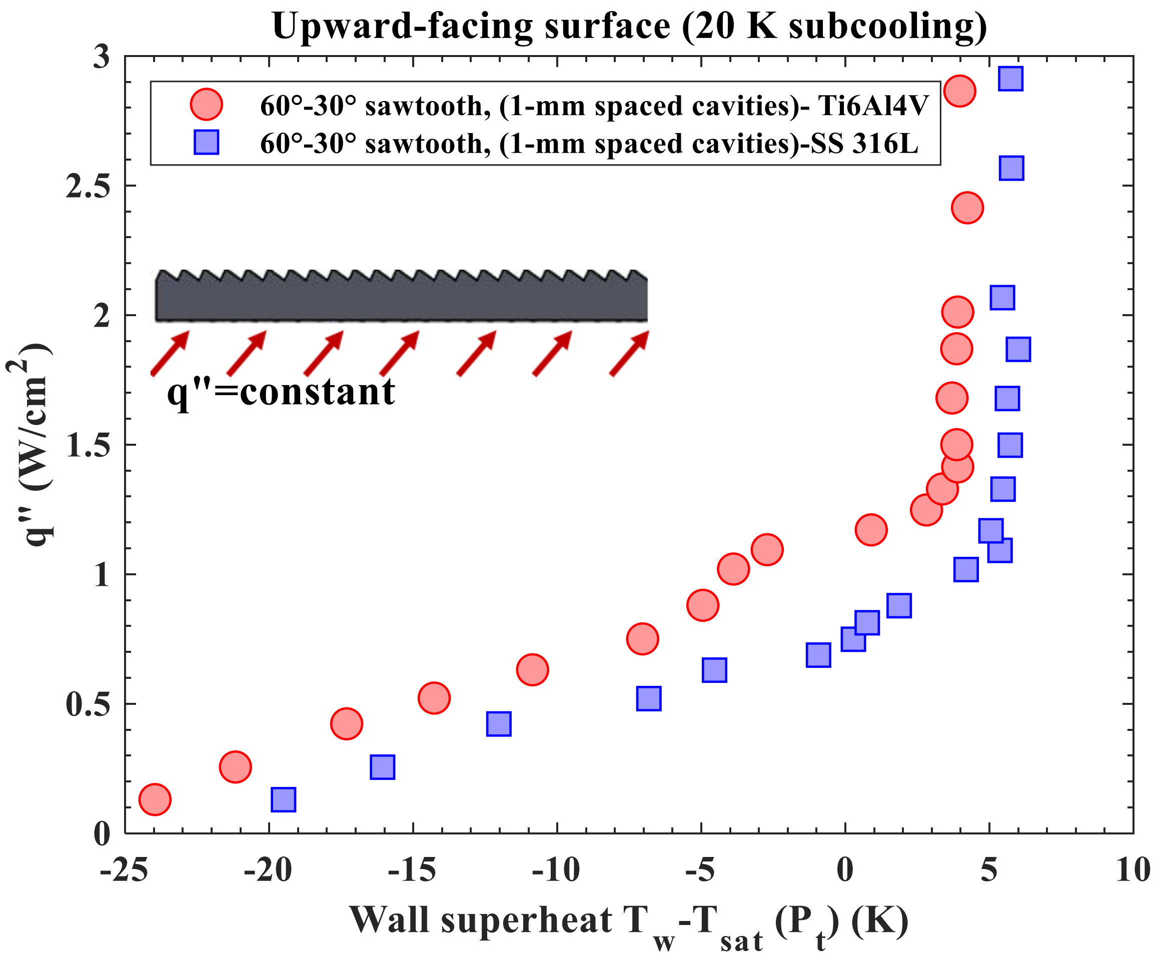

Figure 35: Effect of test surface material on upward-facing surface with a 60°-30° sawtooth structure

The effect of test surface orientation was also investigated for the titanium alloy (Ti-6Al-4V) test surfaces as shown in Fig. As expected, the effect of surface orientation significantly altered boiling behavior as shown in Figure 6. For the downward facing Ti6Al4V surface, nucleation is observed at heat fluxes as low as 0.88 W/cm^2 compared to 1.32 W/cm^2 for the upward facing surface. It is also seen that dryout is observed at 1.96 W/cm^2 for the downward facing surface, while similar dryout conditions were observed for the upward-facing orientation at >3 W/cm^2.

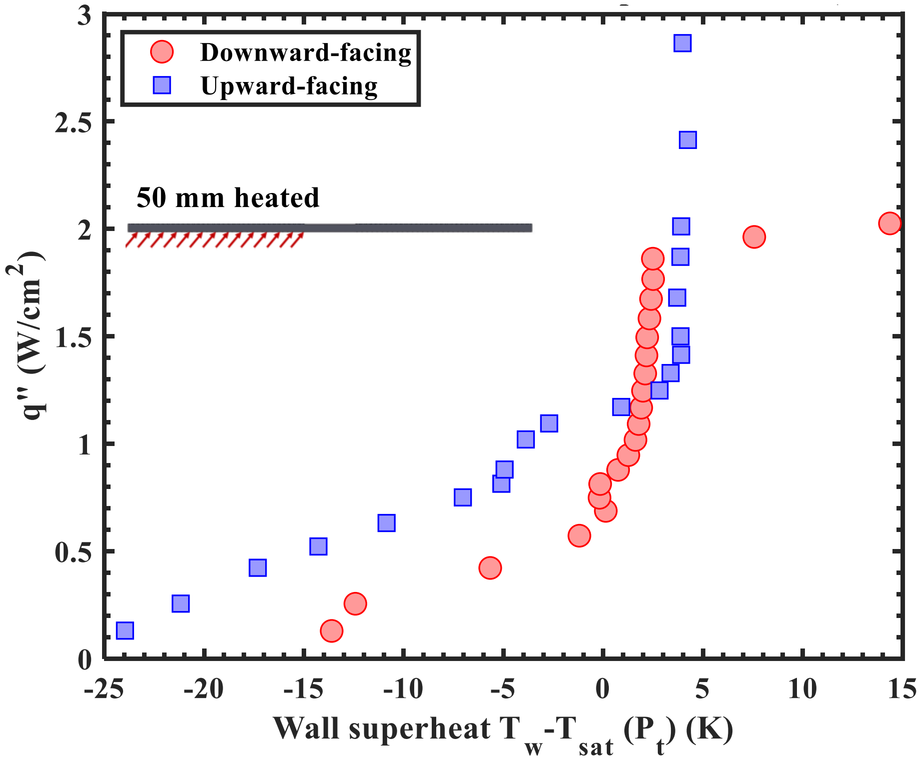

Figure 36: Effect of test surface orientation for a titanium (Ti-6Al-4V) surface with a 60°-30° sawtooth structure

3.7 Effect of heated length on downward-facing surfaces

The effect of heated length was significant for the downward-facing configuration due to vapor production close to the surface. In addition to onset of nucleate boiling at a slightly higher wall superheat, the heat flux required for the onset of nucleate boiling was 0.54 W/cm^2 for the test surface with 100 mm heated compared to 0.7 W/cm^2 for a 50 mm heated length, as shown in the Figure 37. The test surface also tended towards dryout at a heat flux 0.81 W/cm^2 lower than the 50 mm test section.

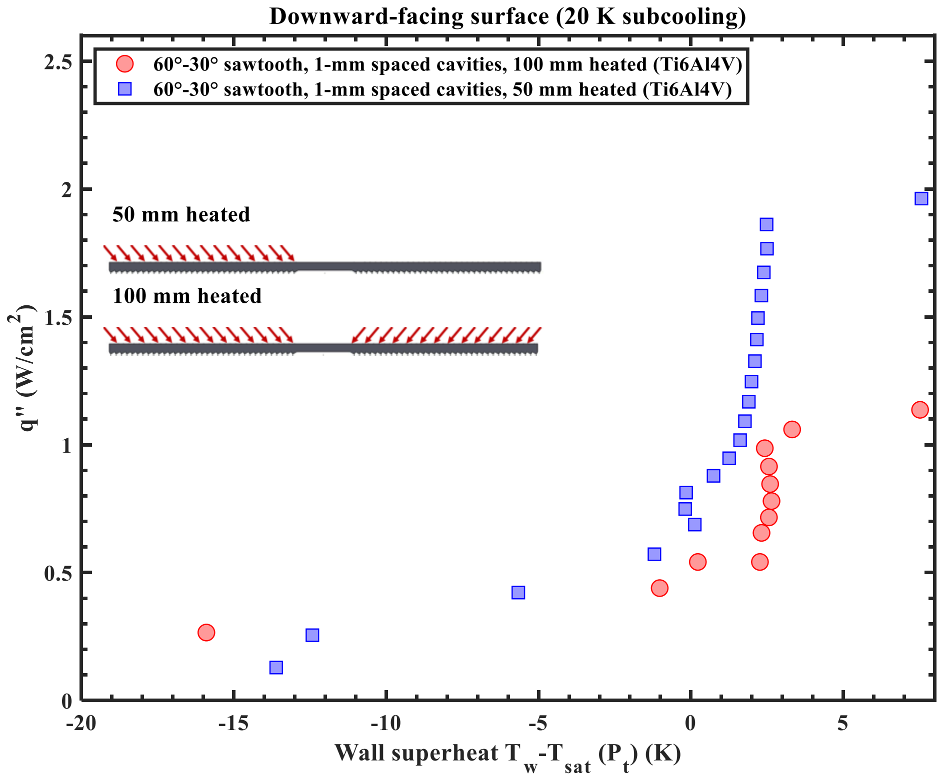

Figure 37: Effect of heated length on downward-facing surfaces with a 60°-30° sawtooth structure.

The significant difference in the dryout heat fluxes is attributed to the increased vapor production with increasing length. Due to increased vapor production, the test surface has a lower inventory of liquid afforded to the liquid-vapor interface, leading to premature dryout. The thicker column of vapor close to the surface also hindered high-speed imaging. Due to these factors, the final test surface length for the microgravity test surface should be maintained at 50 or 80 mm to ensure a wider region of viable heat fluxes.

3.8 Effect of sawtooth structure for upward-facing surface:

For the upward-facing surfaces, the difference in sawtooth structures did not alter the boiling curves significantly as shown in Figure 38. However, the vapor bubbles nucleating from the cavities were influenced at different angles during nucleation and departure as shown in Figure 39. Apart from the differing sawtooth angle, another factor in influencing directional vapor bubble growth can be attributed to the height of the sawtooth structure. As the 75°-15° sawtooth structure allows more room for the vapor bubble to grow, the bubble's directionality is negligibly influenced by neighboring sawtooth in the upward-facing orientation.

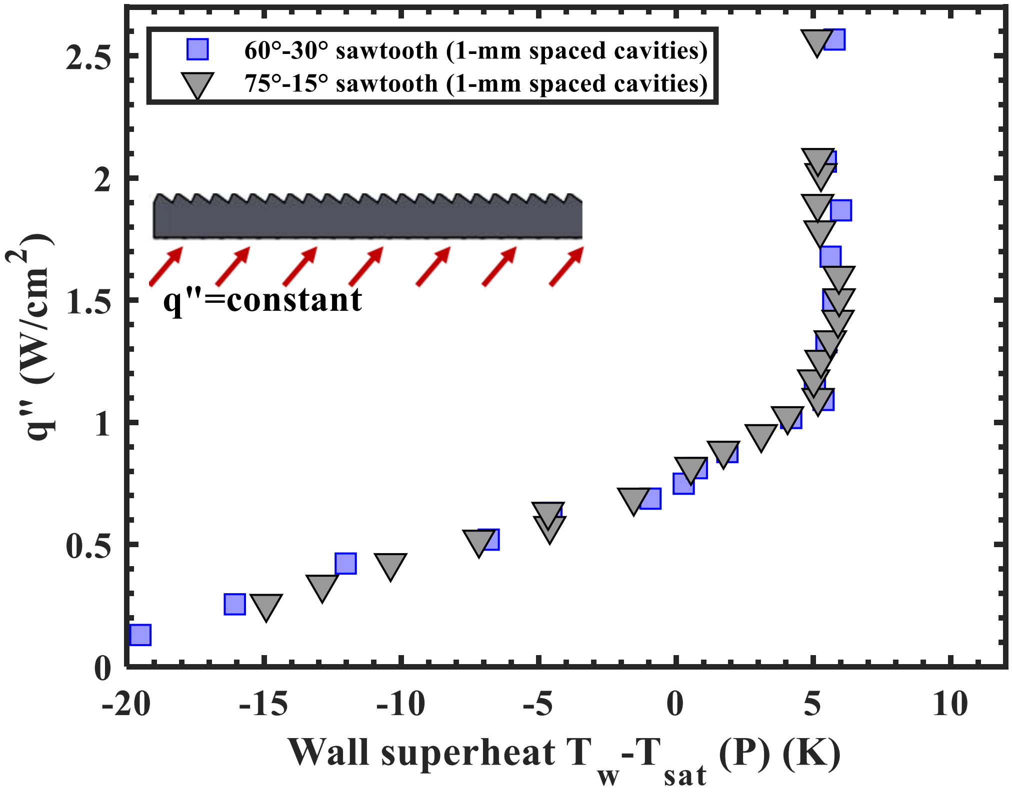

Figure 38: Effect of sawtooth structure for upward-facing test surfaces with 1-mm cavities

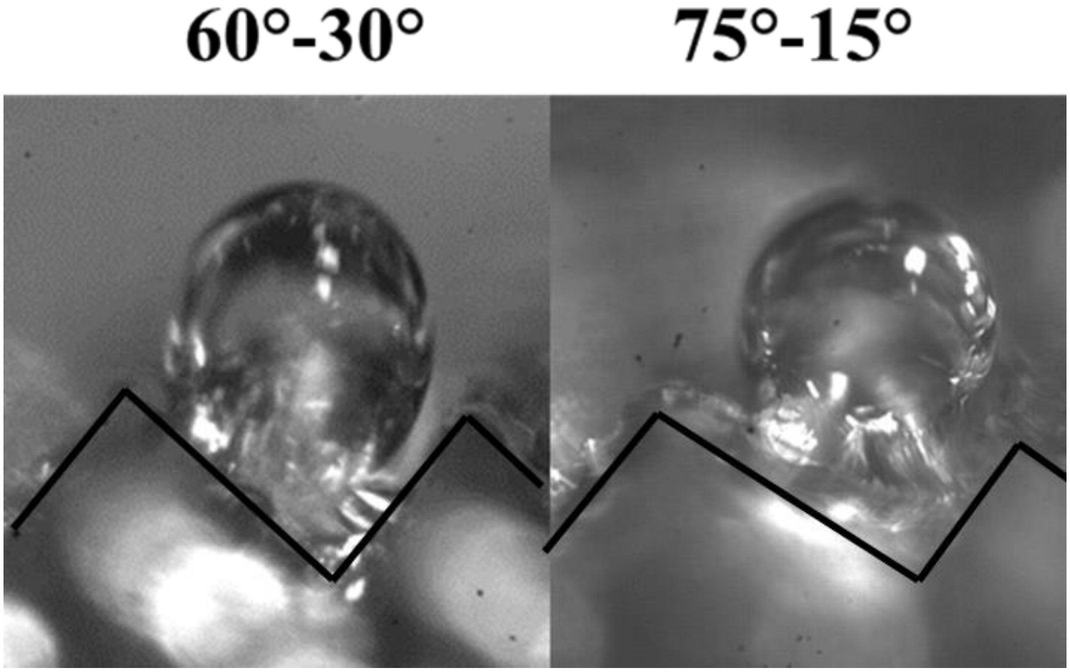

Figure 39: Vapor bubbles influenced in different directions close to the sawtooth surface

3.9 Increase in pressure in the closed system

As mentioned in Chapter 2, the tests discussed in this section were conducted in sub-atmospheric conditions. Another important design consideration for the ISS experiments is the increase in system pressure during the experimental runs. Though vapor bubble dynamics are expected to be different in microgravity conditions, the terrestrial experiments provide a valuable frame of reference for design purposes. Across the variations of experimental runs performed in this study, the highest increase in pressure for the 50 mm test section was 0.216 atm. A sample pressure trace from an upward-facing test surface with a 60°-30° sawtooth structure and 1-mm spaced cavities is shown in Figure 40. The constant rising trend observed in the figure was not observed to change appreciably across the parameters observed in the study.

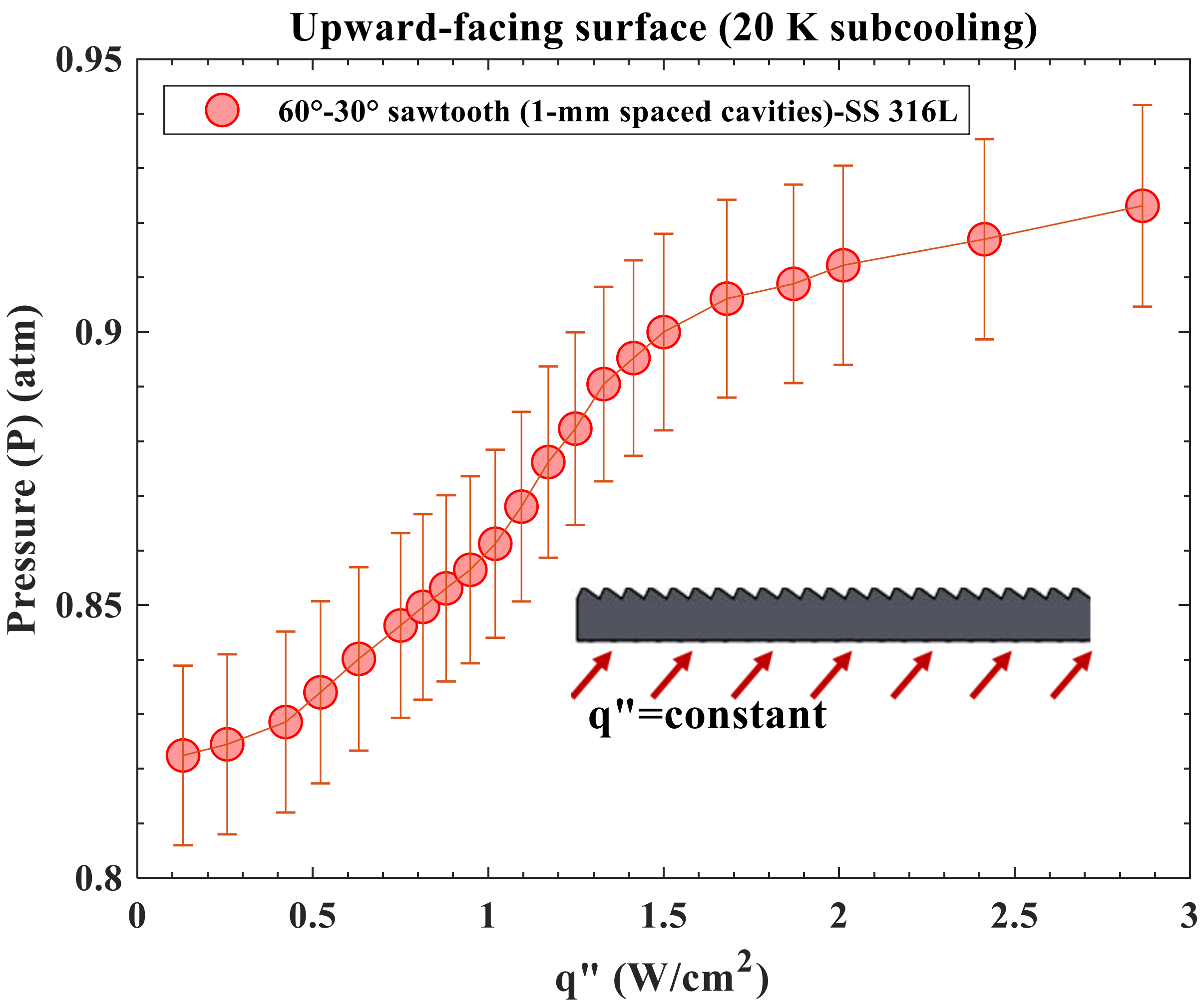

Figure 40: Sample pressure trace observed during the experimental runs

3.10 Baseline test surface observations

A titanium baseline test surface which contained 250 μm cavities but no sawteeth was placed in the experimental setup to observe vapor bubble dynamics. The cavities were spaced 1-mm apart on the test surface. At a heat flux of 0.77 W/cm^2, a series of high-speed images detailed the vapor bubble dynamics in the downward-facing baseline test surface as shown in Figure 41. Vapor bubbles were seen nucleating from the engineered cavities, validating their role as effective nucleation sites on the baseline test surfaces as well. As the vapor bubbles grew larger, neighboring bubbles coalesced to form larger bubbles. It should be noted that these vapor bubbles are not only growing in the x and y direction but in the z direction as well.

With the heat flux remaining constant, the coalesced vapor bubbles further grew on the surface and slowly covered the frame of observation. Finally, the diameter of the flattened bubbles increased to surpass the width of the test surface (6 mm) and slid away in the z-direction (in and out of the plane). During the process of nucleating, coalescing, and sliding, the vapor bubbles oscillated in the x-direction but were not observed moving in any specific direction.

As the heat flux was increased, the above process was repeated in an accelerated timeframe. An increased volume of vapor covered the test surface, rendering chaotic high-speed images. Dryout was observed at a heat flux of 1.36 W/cm^2, compared to a 1.96 W/cm^2 for Ti-6Al-4V test surface with 60°-30° sawtooth with 1-mm spaced cavities. Interestingly, no liquid-vapor interface was observed underneath the flattened bubbles for the baseline test surface. This could be due to a thinner liquid film that could not be observed due to imaging limitations. However, with imaging conditions identical to the microstructure studies, the lack of an interface even with post-processing is surprising

The above results strengthen the need to explore the role of the thin liquid film in motion induced by the microstructure.

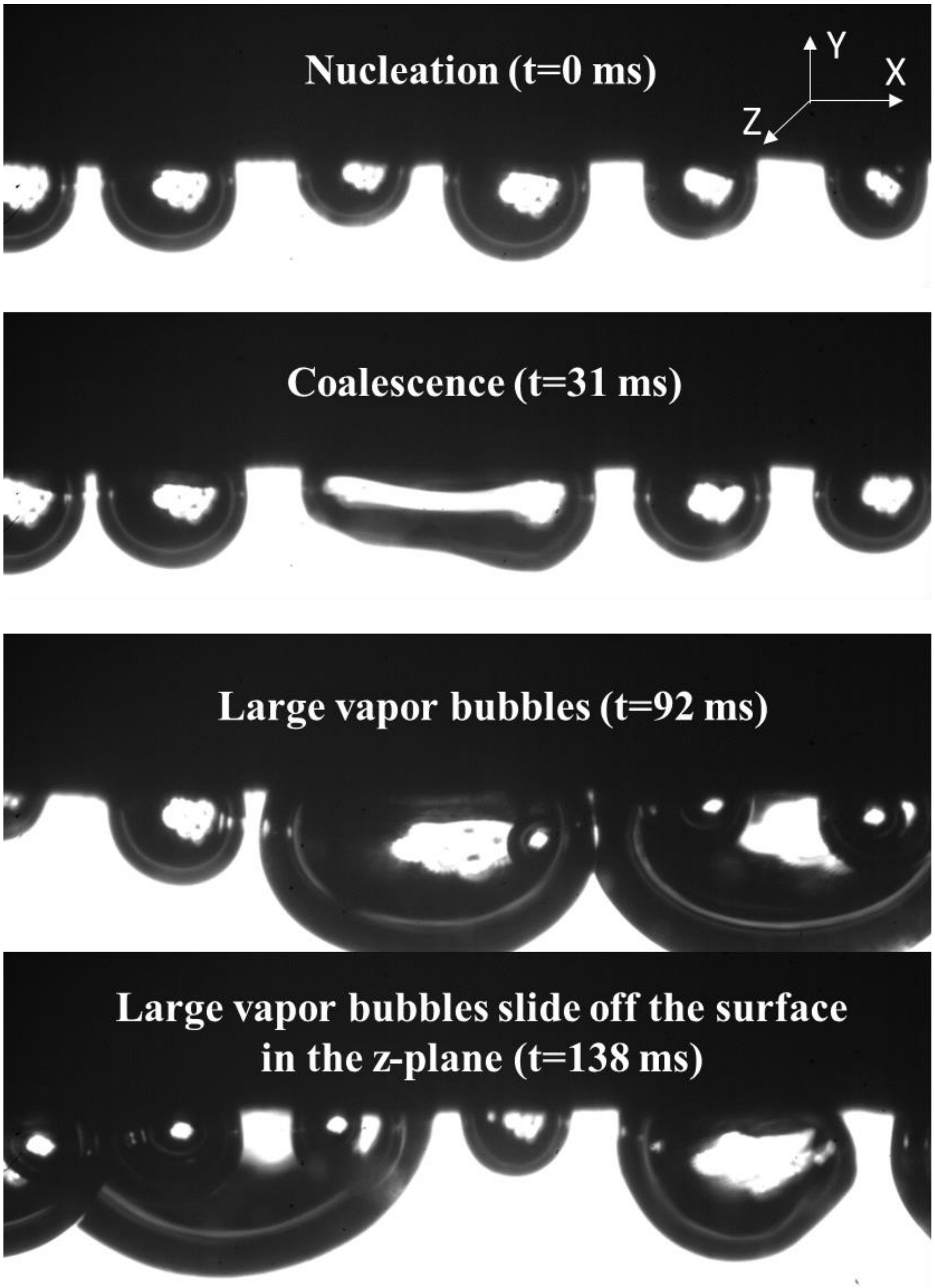

Figure 41: Vapor bubbles nucleating, coalescing and finally outgrowing the baseline test surface to slide off in the z-direction in the downward-facing configuration at 0.77 W/cm^2. The coordinate system for the image sequence is illustrated in the upper right corner. (1280x800, 1000 fps)

3.11 Preliminary liquid film thickness prediction for downward-facing surface through a modified microgravity model

The bubble transit hypothesis for the microstructure, proposed by Thiagarajan et al.[27], performs a force balance on a vapor bubble in microgravity to predict a liquid film thickness from a measured velocity or vice-versa. The hypothesis proposed for the microgravity model was modified to consider the forces on a vapor mass on a downward-facing surface, as shown in Figure 42.

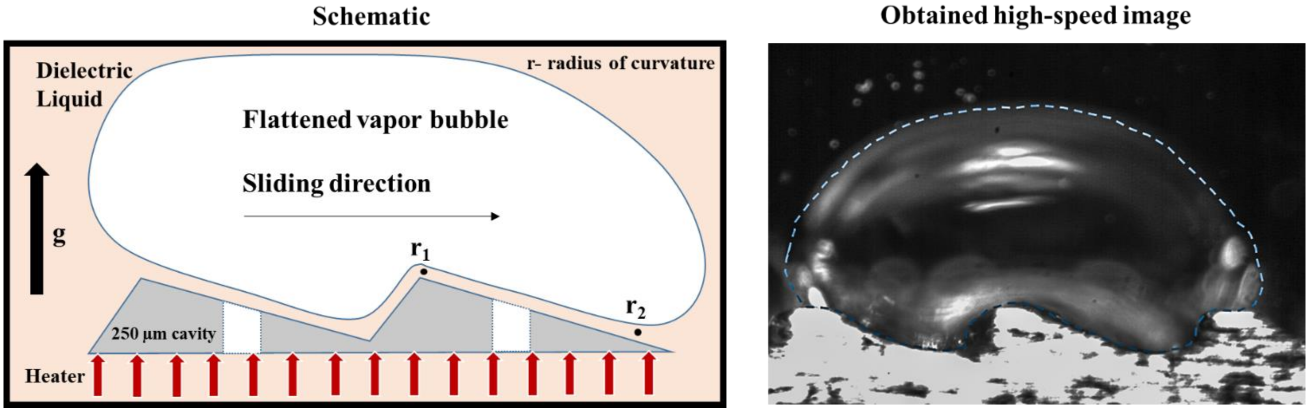

Schematic

Obtained high-speed image

Figure 42: The schematic of the downward-facing, modified model is illustrated along with the example of a high-speed image. The radius of curvature along with the sliding direction of the vapor mass is highlighted. The image orientation is flipped for ease of viewing.

The forces accounted in the primary model include:

1. Pressure differences due to difference in radius of curvature of the liquid-vapor interface between the crest and trough of the sawtooth.

$$F_{\Delta P,tot} = \left\{ m\left[\left(\frac{\mu V}{H} + \frac{H}{2}\frac{\partial P}{\partial x}\right) LW\cos\theta\right]_{long\ slope} - n\left[\left(\frac{\mu V}{H} + \frac{H}{2}\frac{\partial P}{\partial x}\right) LW\sin\theta\right]_{short\ slope} \right\}$$

where, $\frac{\partial P}{\partial x}$ is the pressure gradient between the crest and trough of the sawtooth

H is the liquid film thickness

θ is the angle of sawtooth

L is the length of the liquid film between the surface of saw tooth and vapor bubble

V is the constant velocity at which the vapor bubble is moving

W is the equivalent diameter of the vapor bubble

m is the number of long slopes covered by the vapor bubble

n is the number of short slopes covered by the vapor bubble

2. As the vapor bubble slides along the surface in a pool of dielectric liquid and is adhered to the microstructure through a thin liquid film, Stokes Drag is considered valid for the downward-facing orientation.

$$F_d = 4\pi\mu RV$$

where R is the radius of bubble (R=W/2).

3.11.1 Modifications to the microgravity model

1. The force due to nucleation from the cavities was not considered for the parabolic flight experiments as the bubble growth rates are significantly lower in microgravity compared to terrestrial gravity. To account for the increased bubble frequency of the downward-facing surface, this force was included in the modified model.

   As each vapor bubble nucleating represented a break or perturbation in the liquid film, the momentum transferred was considered as a retarding force to the moving vapor slug. In addition, the high-speed images clearly show that when a vapor bubble nucleates and coalesces with an existing vapor mass, the vapor mass remains stationary and reconstitutes. The force was calculated using a momentum balance calculated by Merte [32]

$$F_v = \pi \sum_{i=1}^{n} \mathrm{D}_{\mathrm{i}}^{\frac{5}{2}} \overline{f_i} \sqrt{\left(\frac{\sigma_i \rho_{v,i}}{3}\right)}$$

where, $\overline{f_i}$ = mean bubble departure frequency, Hz

D_i=bubble departure diameter, m

σ_i =surface tension, N/m

The model attempts to calculate the thermocapillary forces in microgravity by estimating the kinetic energy converted to velocity when two bubbles combine. An important assumption of the model is that ideally, the energy from coalescence is completely converted to kinetic energy. In microgravity, this model assumes importance due to the lack of buoyancy force driving bubble motion. From the measured velocities, it is evident that the retarding forces for motion are higher for the downward-facing surface. To address this increase, a preliminary effort has been made through the process of nucleation and coalescence.

2. The microgravity model was constructed for an isolated spherical bubble in microgravity. In the downward-facing orientation, the bubble is flattened across several sawteeth, rather than just one. To account for this difference in geometry, the resulting liquid film thickness was divided by the number of sawteeth covered by the vapor slug observed. This approximation is an attempt to account for the non-spherical vapor mass geometry.

3. The microgravity experiment was conducted with 60°-30° sawtooth profile while the downward-facing, terrestrial high-speed images were obtained with a 75°-15° sawtooth profile.

3.11.2 Validation of empirical data

At a heat flux of 1.25 W/cm^2, the input data to the model (obtained from high-speed images) included the following along with fluid properties at the saturation temperature:

$$D = 0.0061\ m$$

$$r1 = 0.00028m$$

$$r2 = 0.00038m$$

$$f = 6\ Hz$$

$$V = 13.7\ mm/s$$

$$Number\ of\ sawteeth\ covered\ by\ the\ vapor\ mass = 2$$

Similarly, at a heat flux of 1.78 W/cm^2, the properties of vapor bubble for the model was input as follows:

$$D = 0.0077\ m$$

$$r1 = 0.00029m$$

$$r2 = 0.00035m$$

$$f = 11\ Hz$$

$$V = 21.8\ mm/s$$

$$Number\ of\ sawteeth\ covered\ by\ the\ vapor\ mass = 4$$

The predicted liquid film thickness for the heat fluxes is summarized in *Table 9*. The required vapor bubble properties could not be obtained for a heat flux of 2.5 W/cm^2 due to the vapor bubble exceeding the field of view rendering chaotic high-speed images.

An important assumption of the microgravity model is that the liquid film thickness is uniform across the crest and trough of the sawtooth. However, the high-speed images for the downward-facing surfaces displayed a clear non-uniformity in the thickness of the liquid film across the sawtooth. The liquid film thickness predicted by the modified model for both heat fluxes fall between the measured values on the crest and the trough. While these are preliminary results, it appears the geometry of the flattened bubbles and the constant nucleation across the vapor bubble might play a crucial role in determining liquid film thickness.

The objective of the modified model is to build on the results obtained from the parabolic flight experiments, and not an attempt to provide a comprehensive evaluation of the forces in the downward-facing orientation. The physics of the downward-facing vapor bubbles require further investigation.

The aspects of the model that need to be improved upon include the high sensitivity to changes in velocity and the narrow range of feasibility.

Table 9: Liquid film thickness predicted by the modified model compared to the obtained high-speed images

Input Heat Flux (W/cm^2)	**Average liquid film thickness at crest (μm)**	**Average liquid film thickness at trough (μm)**	**Liquid film thickness predicted by the modified model (μm)**
1.25	46	124	59
1.78	74	180	112

CHAPTER 4 CONCLUSIONS

The borosilicate glass square tube with 8 mm I.D. resulted in the test surface trending towards dryout at heat fluxes as low as ~3 W/cm^2 for the upward-facing configuration and ~2.5 W/cm^2 for the downward-facing configuration. The downward-facing configuration is an attempt to mimic vapor mobility in microgravity conditions as buoyancy forces do not detach vapor bubbles from the surface. Vapor mobility actuated by the microstructure was observed for the downward-facing surface with distinct features such as nucleation, coalescence, and subsequent sliding of the vapor bubbles. A thin liquid film was observed above the coalesced bubbles (between the vapor and the solid downward facing surface) and the thickness of the liquid film varied depending on the location at the sawtooth. The trough had a higher thickness than the crest for the conditions encountered in the study. The liquid film thickness for the vapor bubbles was also found to increase with increasing heat fluxes for the 75°-15° sawtooth structure. In contrast, a baseline test surface with no microstructure showed stagnant vapor bubbles that grew large enough to surpass the width of the test surface. A model for predicting the liquid film thickness was presented by modifying a force balance model from a previous NASA Zero-G flight experiment. The effect of nucleation site density was significant for the upward-facing configuration, resulting in a difference in superheat of 4.5 K during nucleation incipience. The discussed sawtooth microstructure is a feasible surface modification to passively enable phase-change cooling for spacecraft electronics.

Preparations for microgravity studies:

To better understand the vapor bubble dynamics afforded by the microstructure in microgravity conditions, preparations for the microgravity experiments are currently underway.

The payload for the experiment is on track to be launched on SpaceX CRS-21, scheduled for October 2020. The team is currently working in close collaboration with Techshot, a NASA Implementation Partner, to meet the requirements of the microgravity studies.

Objectives for the microgravity experiments include:

I. Verify lateral bubble motion under low jitter and long duration low g conditions aboard ISS lab. Tasks associated with this objective include the following

1. Development of detailed design criteria and parameters for the ISS PFMI ampoule design by conducting terrestrial experiments on a modified open-ended channel facility
2. Terrestrial verification of modified PFMI ampoule and test procedure development- Fabricate a prototype ampoule and verify its performance in terrestrial gravity in a modified PFMI set up at Techshot
3. Launch package preparation & communication link setup - Multiple test ampoules will be fabricated and the team will work with Techshot to support launch package development and communication link establishment at Auburn
4. Data collection from ISS lab experiment- sensor and high-speed image data will be collected toward verification of lateral bubble motion

II. Validate and refine the steady state bubble motion model based on ISS and terrestrial data- Data from the ISS lab experiment and terrestrial experiments will be used to verify and refine the terrestrial model

REFERENCES

[1] "ITRS Reports - International Technology Roadmap for Semiconductors." [Online]. Available: http://www.itrs2.net/itrs-reports.html. [Accessed: 11-Feb-2020].

[2] J. Wu, Y.-L. Shen, K. Reinhardt, H. Szu, and B. Dong, "A Nanotechnology Enhancement to Moore's Law," *Appl. Comput. Intell. Soft Comput.*, vol. 2013, p. 13, 2013.

[3] "Cooling System Keeps Space Station Safe, Productive | NASA." [Online]. Available: https://www.nasa.gov/content/cooling-system-keeps-space-station-safe-productive. [Accessed: 01-Jul-2020].

[4] S. Nukiyama, "The maximum and minimum values of the heat Q transmitted from metal to boiling water under atmospheric pressure."

[5] F. P. Incropera and D. P. DeWitt, *Fundamentals of Heat and Mass Transfer*. 1996.

[6] T. M. Anderson and I. Mudawar, "Microelectronic Cooling by Enhanced Pool Boiling of a Dielectric Fluorocarbon Liquid," 1989.

[7] V. Carey, *Liquid vapor phase change phenomena: an introduction to the thermophysics of vaporization and condensation processes in heat transfer equipment*. 2018.

[8] K. G. Rajulu, R. Kumar, B. Mohanty, and H. K. Varma, "Enhancement of nucleate pool boiling heat transfer coefficient by reentrant cavity surfaces," *Heat Mass Transf. und Stoffuebertragung*, vol. 41, no. 2, pp. 127–132, Dec. 2004.

[9] N. Nimkar, S. Bhavnani, R. J. of heat and mass Transfer, and U. 2006, "Effect of nucleation site spacing on the pool boiling characteristics of a structured surface," *Elsevier*.

[10] S. Bhavnani *et al.*, "Boiling Augmentation with Micro/Nanostructured Surfaces: Current

Status and Research Outlook," *Nanoscale Microscale Thermophys. Eng.*, vol. 18, no. 3, pp. 197–222, Jul. 2014.

[11] L. Dong, X. Quan, and P. Cheng, "An experimental investigation of enhanced pool boiling heat transfer from surfaces with micro/nano-structures," *Int. J. Heat Mass Transf.*, vol. 71, pp. 189–196, Apr. 2014.

[12] X. Zheng and C. W. Park, "Experimental study of the sintered multi-walled carbon nanotube/copper microstructures for boiling heat transfer," *Appl. Therm. Eng.*, vol. 86, pp. 14–26, May 2015.

[13] K. H. Chu, R. Enright, and E. N. Wang, "Structured surfaces for enhanced pool boiling heat transfer," *Appl. Phys. Lett.*, vol. 100, no. 24, Jun. 2012.

[14] C. D. Ghiu and Y. K. Joshi, "Visualization study of pool boiling from thin confined enhanced structures," *Int. J. Heat Mass Transf.*, vol. 48, no. 21–22, pp. 4287–4299, Oct. 2005.

[15] Y. Fujita, H. Ohta, S. Uchida, and K. Nishikawa, "Nucleate boiling heat transfer and critical heat flux in narrow space between rectangular surfaces," *Int. J. Heat Mass Transf.*, vol. 31, no. 2, pp. 229–239, 1988.

[16] A. Priarone, "Effect of surface orientation on nucleate boiling and critical heat flux of dielectric fluids," *Int. J. Therm. Sci.*, vol. 44, no. 9, pp. 822–831, Sep. 2005.

[17] K. N. Rainey and S. M. You, "Effects of heater size and orientation on pool boiling heat transfer from microporous coated surfaces," *Int. J. Heat Mass Transf.*, vol. 44, no. 14, pp. 2589–2599, Jun. 2001.

[18] J. Y. Chang and S. M. You, "Boiling heat transfer phenomena from micro-porous and

porous surfaces in saturated FC-72," *Int. J. Heat Mass Transf.*, vol. 40, no. 18, pp. 4437–4447, Nov. 1997.

[19] M. Chan Jo, "Thermally Actuated Pumping of a Single-phase Fluid using Surface Asymmetry," 2008.

[20] A. D. Stroock, R. F. Ismagilov, H. A. Stone, and G. M. Whitesides, "Fluidic Ratchet Based on Marangoni-Bé nard Convection," 2003.

[21] H. Linke *et al.*, "Self-propelled leidenfrost droplets," *Phys. Rev. Lett.*, vol. 96, no. 15, 2006.

[22] G. Dupeux, M. Le Merrer, G. Lagubeau, C. Clanet, S. Hardt, and D. Quéré, "Viscous mechanism for Leidenfrost propulsion on a ratchet," *EPL*, 2011.

[23] F. Kapsenberg, N. Thiagarajan, V. Narayanan, and S. Bhavnani, "Lateral motion of bubbles from surfaces with mini ratchet topography modifications during pool boiling- experiments and preliminary model," *Intersoc. Conf. Therm. Thermomechanical Phenom. Electron. Syst. ITHERM*, pp. 165–175, 2012.

[24] Y. F. Xue, J. F. Zhao, J. J. Wei, J. Li, D. Guo, and S. X. Wan, "Experimental study of nucleate pool boiling of FC-72 on smooth surface under microgravity," *Microgravity Sci. Technol.*, 2011.

[25] R. Raj, J. Kim, and J. McQuillen, "Pool Boiling Heat Transfer on the International Space Station: Experimental Results and Model Verification," *J. Heat Transfer*, 2012.

[26] G. R. Warrier, V. K. Dhir, and D. F. Chao, "Nucleate pool boiling eXperiment (NPBX) in microgravity: International space station," *Int. J. Heat Mass Transf.*, 2015.

[27] N. Thiagarajan, S. H. Bhavnani, and V. Narayanan, "Self-Propelled Sliding Bubble Motion Induced by Surface Microstructure in Pool Boiling of a Dielectric Fluid Under

Microgravity," 2015.

[28] W. E. King *et al.*, "Laser powder bed fusion additive manufacturing of metals; physics, computational, and materials challenges," *Appl. Phys. Rev.*, vol. 2, no. 4, p. 041304, Dec. 2015.

[29] R. A. Stivey, S. Gilley, A. Ostrogorsky, R. Grugel, G. Smith, and P. Luz, "SUBSA and PFMl transparent furnace systems currently in use in the International Space Station Microgravity Science Glovebox," 2003.

[30] C. A. Schneider, W. S. Rasband, and K. W. Eliceiri, "NIH Image to ImageJ: 25 years of image analysis," *Nature Methods*, vol. 9, no. 7. pp. 671–675, Jul-2012.

[31] M. J. Donachie, "Titanium A Technical Guide Second Edition," 2000.

[32] H. Merte, "Momentum effects in steady nucleate pool boiling during microgravity," *Ann. N. Y. Acad. Sci.*, vol. 1027, pp. 196–216, 2004.

[33] T. Beckwith, R. Marangoni, and J. Lienhard, "Mechanical Measurements," 2009.

APPENDIX A

Proof-of-concept experiment

A proof-of-concept experiment was conducted initially to verify the passive bubble motion facilitated by the surface microstructure. A test section with dimensions of 40 mm x 20 mm x 2 mm was printed with 250 µm and 500 µm cavities and subsequently heated in a test chamber to verify bubble motion.

For the passive bubble transport hypothesis to be valid, it is essential that bubble nucleation is exclusively from the fabricated nucleation sites. Microscopic highs or peaks on the surface of the saw-toothed structure could act as potential nucleation sites, obscuring the intended transport. The extraneous bubbles formed at the peaks will not have any initial horizontal velocity component and will not experience the pressure differential. Therefore, these bubbles will not have any preferential motion. Reducing the surface roughness becomes important to reduce the number of potential nucleation sites, particularly along the peaks of the saw-toothed structure. Surface roughness measurements along the peak and the gradual slopes were determined using a Keyence Digital Microscope -VHX-1000. The microscope compiles a fully focused 3D image by varying the focus distance along the height range of the peaks. These 3D images give a graph of the height profile of the structure, allowing for surface roughness to be calculated. For each test surface, measurements along three different peaks were taken and averaged together. In this project, the root mean squared (RMS) surface roughness is used with a target of 10 to 20 µm, a target derived from projects with similar heating characteristics. The RMS surface roughness is calculated using the equation:

$$R_{RMS} = \sqrt{\sum_{i=1}^{n}(Z_i - Z_{mean})^2}$$

where Z_i is the height of each point from 1 to n and Z_{mean} is the average surface height.

First, the test surfaces were sandblasted in a sandblasting cabinet using 180 grit aluminum oxide blasting media. Test surfaces were sandblasted for 5 seconds and 30 seconds to determine if a longer or shorter time provides a better surface roughness. While the sandblasting provided much better visual appearance, the method did not actually reduce the surface roughness at the peaks. This was probably due to the harsh nature of sandblasting. At the peaks of the surface, the media can easily cut into the peak due to the small amount of original material at the sharp edge, leaving craters and large indentions that can act as unwanted nucleation sites.

The second method involves electropolishing, a method that takes off microscopic layers of material by passing an electrical current through the test surface while placed in an electrolyte solution. This method is the opposite of electroplating, where the workpiece is the anode. The process removes workpiece material much faster at microscopic peaks rather than valleys, smoothing out the surface and removing the oxidized layer. To remove the oxidized layer and improve the surface finish, the test surfaces were placed in an electropolishing apparatus, consisting of a phosphoric acid bath, a metal anode placed in the bath, and the test surface as a cathode connected to a 35V power source. Electropolishing creates an ion boundary layer around the piece which removes small amounts of material from the outermost layer, smoothing out microscopic peaks on the surface microstructure. The test surface was originally polished for 10 minutes at 35V, followed by more polishing for 20 additional minutes. The electropolishing achieved better roughness characteristics at the maximum voltage and time used. At 20V and 10 minutes, one side of the specimen’s surface roughness was measured at 17.912 µm showing the potential of electropolishing, which in this case, reduced the surface roughness by almost 10 µm. Further optimization of this process will be implemented in the future with longer polishing times, higher voltage, and a more even current distribution along the test surface.

The pool apparatus consisted of a borosilicate square tube superglued to a polycarbonate base and lid. The glued top was open to allow for access to the specimen but contained four ¼”-20 screws and a gasket to screw on a polycarbonate lid for operation. A Graham condenser with a recirculating chiller was attached to the top of the apparatus to prevent any FC-72 vapor from escaping to the atmosphere.

A cartridge heater was placed inside of an insulated round copper bar to provide the power. The cartridge heater was 250W, 120V, 3.2 mm diameter and 32 mm in length. The copper was specially machined into a flange-like structure, insulated and screwed into the bottom of the bottom Lexan piece, using a gasket to prevent any leaks. The top of the copper block protruded through the Lexan piece to contact the specimen, providing virtually one-dimensional conduction of most of the heater wattage. The heater was then powered using a variable 60V power supply. The specimen was attached to the copper block by Arctic Silver thermal paste (99.9% pure micronized silver) to provide a good thermal interface. The surrounding of the piece and the copper was covered with high temperature silicone RTV as shown in Figure 43, preventing the FC-72 from leaking, or touching the copper, which would cause many extraneous bubbles and skew the results. The high-speed camera used was the Phantom v310 with a close-up C4 lens. The complete experimental setup is shown in Figure 43 and Figure 44. Figure 45 shows the bubble nucleation from neighboring ratchets.

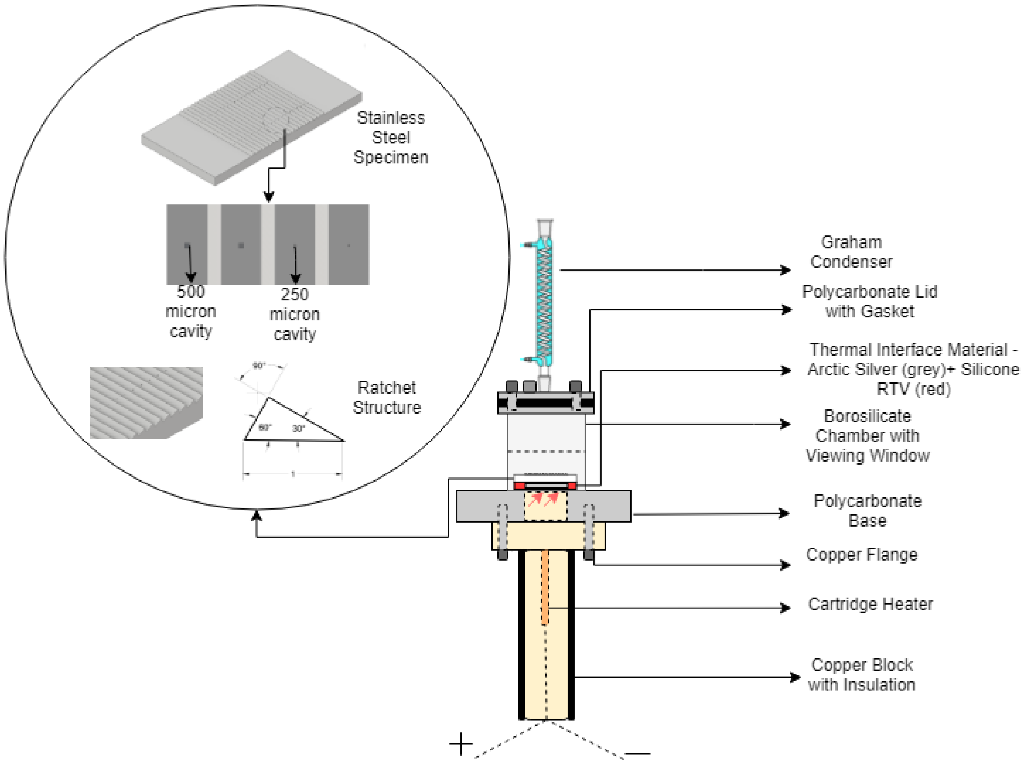

Figure 43: Proof-of-concept experiment set-up showing details of the chamber, test surface, and heat source

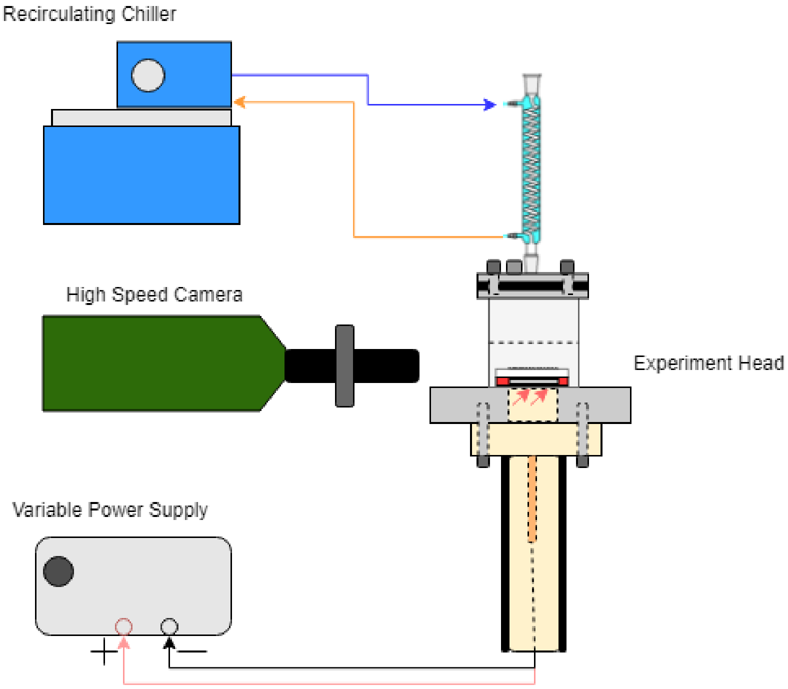

Figure 44: Auxiliary equipment used in the experiment

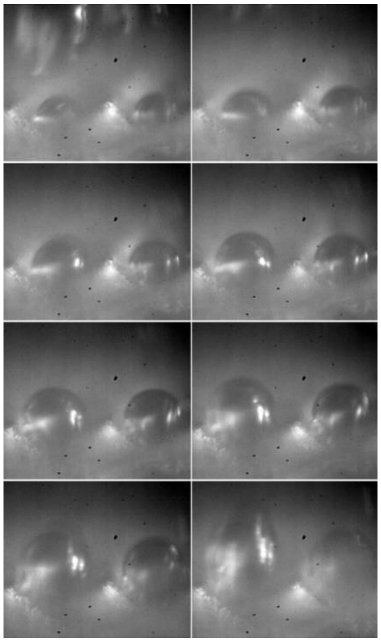

Figure 45: Series of images showing bubble nucleation and departure from a pair of nucleation sites. All images taken at an interval of 3.33 milliseconds from 250 µm cavities.

Bubble diameter was measured from the sequence of captured high-speed images using the ImageJ software. The high-speed images were captured at a resolution of 1280x720 at 3488 fps. The scale for the images was calibrated using the peaks of the sawtooth ratchet which were 1 mm apart from each other. A clear frame of the bubble departing from the surface was chosen as the reference frame. The bubble under focus was measured again after 20 milliseconds to measure the change in diameter. Both bubble diameter and frequency observations were made under constant heat flux with the cartridge heater providing 30W. From the obtained sequence of images, six bubbles with clear trajectories were studied from the small and large cavities each.

The bubble departure diameters were observed to be a strong function of the cavity sizes. The smaller cavity size yielded an average bubble departure diameter of 0.32 mm and the larger cavity size yielded a bubble departure diameter of 0.58 mm immediately after departure. Within the viewing window, these bubbles grew to an average of 0.4 mm and 0.64 mm respectively, 20 milliseconds after departure as shown in Figure 46 and Figure 47.

The bubble departure frequency was found to vary with the cavity sizes as well. The smaller cavity size yielded a bubble departure frequency range of 38-40 Hz while the larger cavity was observed to have a lower frequency range at 23-25 Hz over the range of observations.

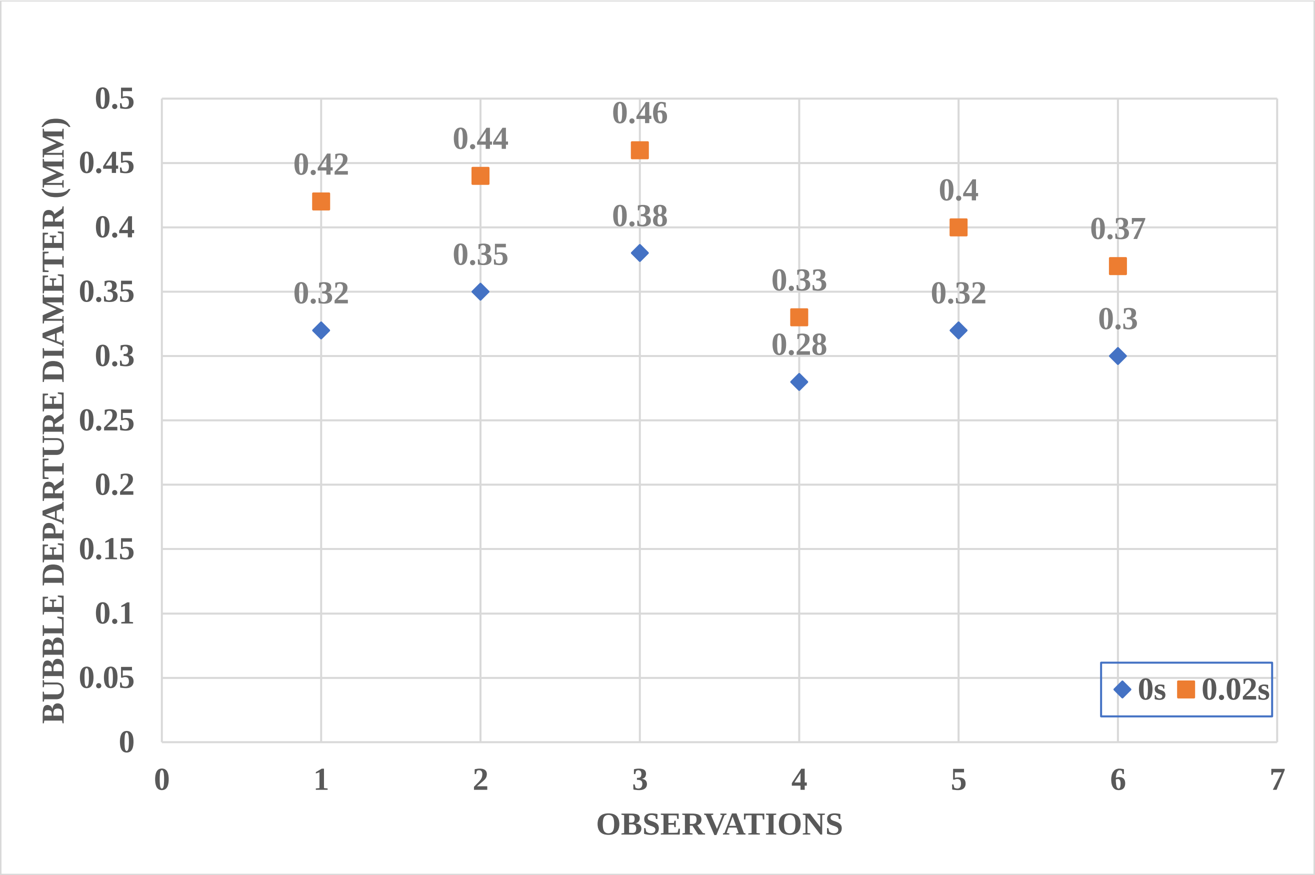

Figure 46: Bubble departure diameter and growth from the smaller cavity over 20 milliseconds

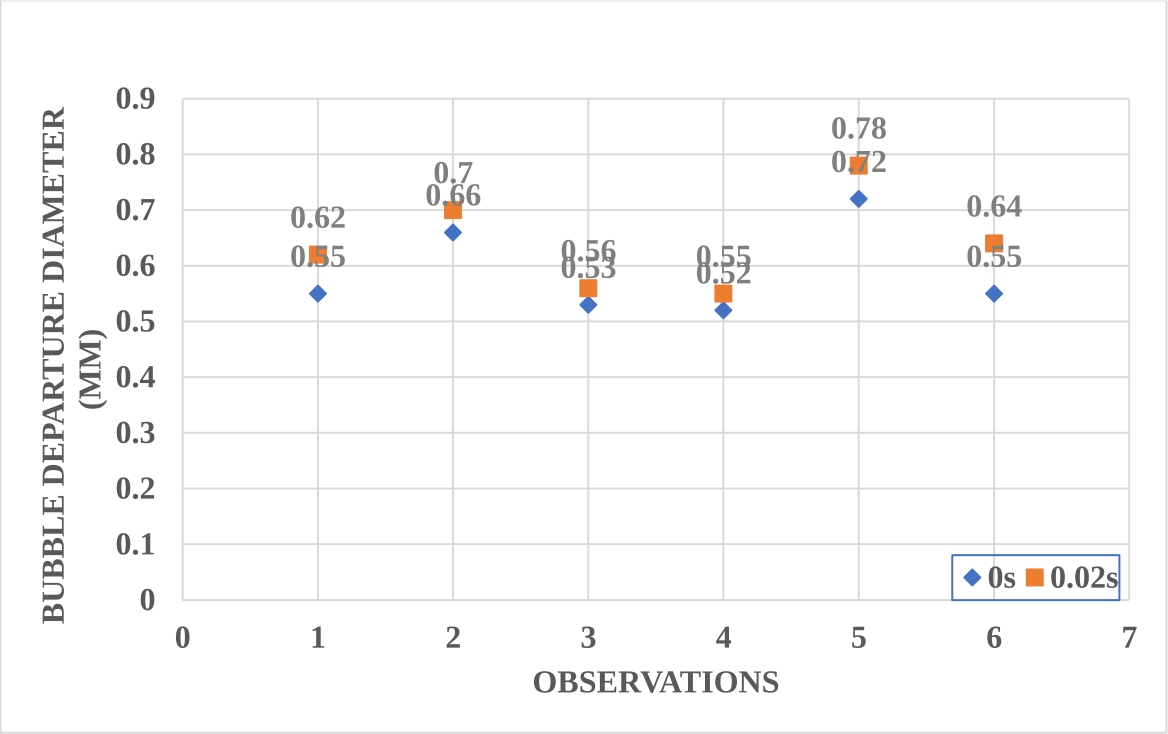

Figure 47: Bubble departure diameter and growth from the larger cavity over 20 milliseconds

The nucleation sites of both sizes were found to be effective when uniform heat flux was applied to the specimen. The size of the vapor bubbles observed from the sites was found to be proportional to the size of the corresponding nucleation site. The 500 μm cavity size was found to produce bubbles large enough to be influenced by neighboring sawtooth ratchets. Higher fluxes were observed to produce extraneous nucleation sites, irrespective of the relative roughness of the surface at those locations. Extraneous nucleation sites were few and limited to the center of the specimen which receives the highest heat flux from the copper block. The bubble departure diameter and frequency were strong functions of the nucleating cavity size.

In subsequent manufacturing runs, the larger cavity size will be reduced to minimize the effect of the neighboring ratchets. Higher electropolishing times do not necessarily translate to a lower number of extraneous nucleation sites, quantitatively. The activation of extraneous nucleation sites from the surface is proportional to the heat flux provided to the specimen. Better lighting and focus of the high-speed images will be achieved for the next phase of the prohect. Metals such as stainless steel and titanium will be tested for favorable glass-to-metal bonds. Equidistant thermocouple wells will be drilled into the copper flange to extrapolate the surface temperature and study the effects of subcooling.

APPENDIX B

Maximum Stress Analysis in Borosilicate Glass Tube

The ratcheted specimens and FC-72 fluid will be contained inside a Dow Corning 7052 borosilicate glass tube during the experiment. Due to the increase in temperature and therefore pressure in the tube, the glass must be tested to withstand a maximum design pressure within a safety factor of 3. This analysis models the borosilicate tube in Solidworks and simulates the stresses in the tube for a range of internal pressures to find the maximum pressure the tube can withstand.

Finite Element Analysis:

While several thicknesses and cross sections of glass tubes are being considered for the specimen, only a 10.6 mm outer width tube of .8 mm thick was modeled because it was the most conservative approach. The circular or thicker cross sections inherently resist stress more effectively and were therefore not considered the limiting factor. The tube was capped with a flat piece of glass at either end, simulating the end conditions of the final glass tube configuration. Again, this is a more conservative approach, as the relatively sharp edges in the model cause higher stress concentrations that will not be evident in the final product. The model is shown in Figure 48.

Figure 48: Borosilicate glass tube model

For the simulation, a high pressure was placed on the inside faces of the tube with atmospheric pressure placed on the outside. One face was held fixed, simulating the holding configuration in the PFMI hardware. A static study calculated the maximum principle stress along the tube, shown in Figure 49. The maximum principal stress failure theory used in this study is the most conservative theory for brittle materials.

When placed under an internal load of 217.5 psi, or 15 times atmospheric pressure, the highest principal stress experienced was 14 psi compared to the ultimate tensile strength of borosilicate glass at 41 psi, resulting in a safety factor of 2.91. This internal pressure is much higher than any pressure expected to occur from the experiment. Therefore, both round and square cross sections thicker than .8mm are within the pressure requirements and should not fail.

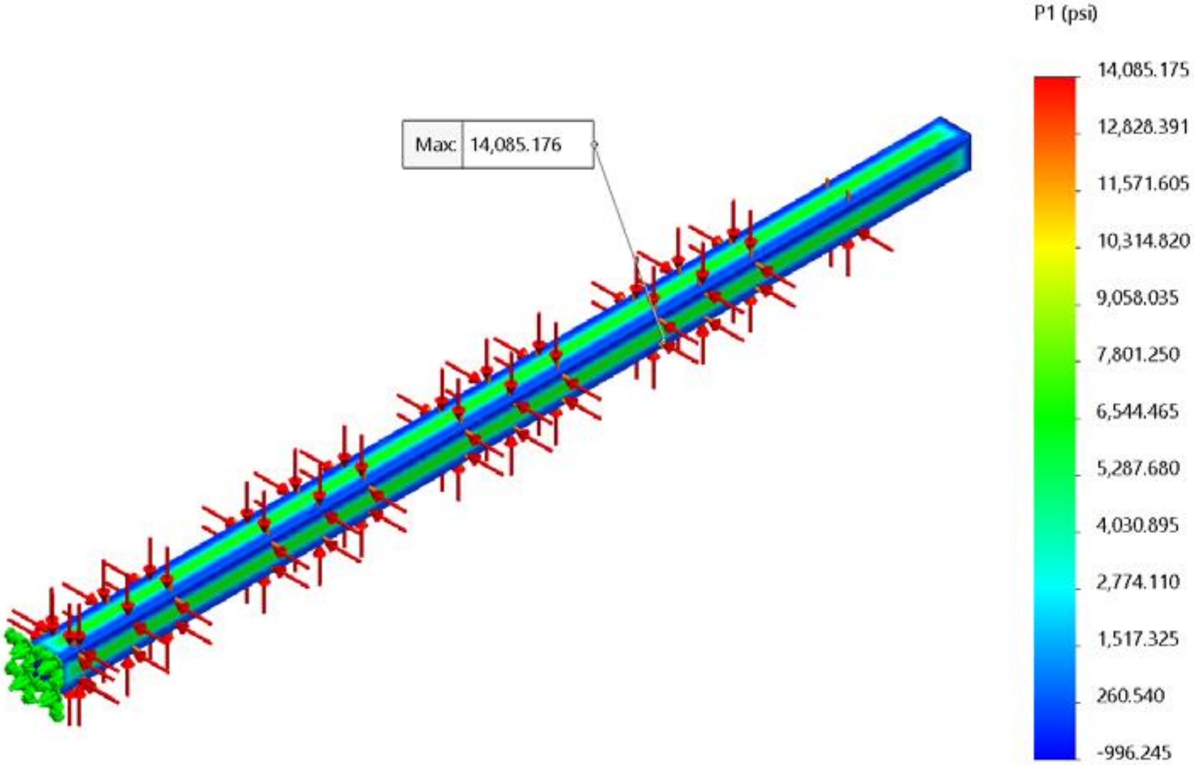

Figure 49: Stress analysis on the borosilicate glass tube model

APPENDIX C

Uncertainty analysis

The primary measured values were measured for uncertainty in this section.

Beckwith et al. [33] reported the uncertainty of a given function as the summation of discrete uncertainties described by the following equation:

$$U_f = \sqrt{\left(U_{x1}\ \left(\frac{\partial f}{\partial x1}\right)\right)^2 + \left(U_{x2}\ \left(\frac{\partial f}{\partial x2}\right)\right)^2 + \cdots + \left(U_{xn}\ \left(\frac{\partial f}{\partial xn}\right)\right)^2}$$

Where U_f is the uncertainty of the function resulting from independent uncertainties

U_{xi} are the uncertainties resulting from discrete sources

x_i are the independent measured variables

From the above equation, the uncertainty in measured heat flux can be described as:

$$\left(\frac{\mathrm{U_q}''}{\mathrm{q}''}\right) = \sqrt{\left(\frac{\mathrm{U_v}}{\mathrm{V}}\right)^2 + \left(\frac{\mathrm{U_I}}{\mathrm{I}}\right)^2}$$

The uncertainty data for the power supply and digital meter were obtained from manufacturer’s specifications.

Uncertainty in voltage measured:

Uncertainty of Keysight - Agilent HP 6632B Power Supply: ±10 mV

Uncertainty of multimeter: ±3 mV

Therefore, $U_v = \sqrt{10^2 + 3^2} = 10.44\ mV$

Uncertainty in current measured:

Uncertainty of Keysight - Agilent HP 6632B Power Supply: ±2 mA

Uncertainty of multimeter: ±1.1 mA

Therefore, $U_I = \sqrt{2^2 + 1.1^2} = 2.28\ mA$

For an input voltage of 15.063 V and input current of 0.3827 A, the calculated heat flux was 1.15 W/cm^2. The area of the heater is 5 cm^2. The resultant uncertainty in heat flux was found to be:

$$U_{q''} = q'' \times \left(\sqrt{\left(\frac{0.01044}{15.063}\right)^2 + \left(\frac{0.00228}{0.3827}\right)^2} \right) = \pm 0.00605 \frac{W}{cm^2}$$

Other uncertainties from the experiment and their sources are reported in Table 10.

Table 10: Uncertainty of measured values in the experimental study

Variable	**Source**	**Uncertainty**
Pressure	Manufacturer’s specification	±2%
Temperature	Student T-distribution (calculated)	±1.6%
Bubble velocity	Observation	±0.5%
Bubble frequency	Observation	±5%

APPENDIX D

Calibration of thermocouples

The thermocouples used in the experiment were calibrated against a NIST-traceable thermistor in an oven where the temperature was increased from 40°C to 100°. Sample calibration data is shown in Figure 50.

The equations from the calibration curves were used to correct the obtained data against the thermistor for each k-type thermocouple. The calibration data was also used to calculate the uncertainty for temperature using student T-distribution in Appendix C. 95% confidence interval was used for the calculations.

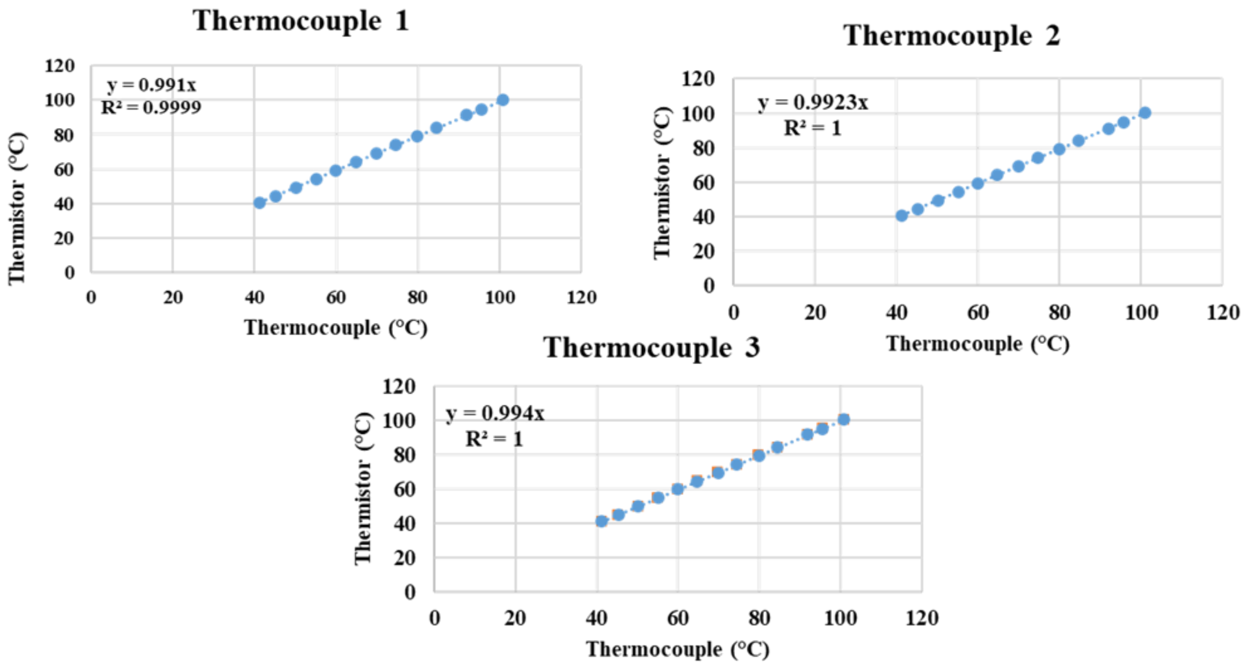

Figure 50: Calibration of thermocouples using a NIST-traceable thermistor

APPENDIX E

Central cold spot hypothesis with upward-facing surfaces

A few experimental runs were conducted with a cold spot in the center of borosilicate tube to test the hypothesis of vapor bubble nucleation, departure and migration to the center as illustrated in Figure 51. Conceptually, to prove the hypothesis, vapor bubbles would be seen nucleating and migrating towards the central cold spot from either heated side. To achieve this, a delicate balance in the heat provided versus the heat dissipated by the cold spot was required. As a result, the cold spot was created using two experimental runs using the following devices- a thermoelectric cooler and a chilled waterblock.

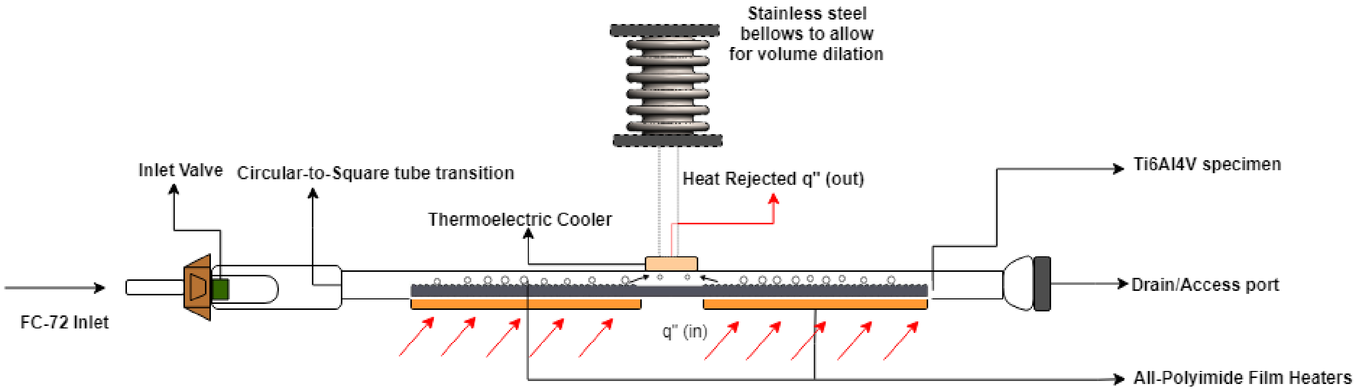

Figure 51: Schematic showing the hypothesis to be tested indicating nucleation, departure, and migration of vapor bubbles to the central thermoelectric cooler

Cold spot with Thermoelectric Cooler

Repeatability runs were conducted for a 75°-15° sawtooth specimen with cavities located on every sawtooth to ensure agreement of obtained data. The boiling curve (Figure 52), and the bulk fluid subcooling (Figure 53) exhibited tight agreement between runs, ensuring closeness of obtained data under identical conditions. During these runs, the thermoelectric cooler (TEC) was set up to provide around 1W cooling with the hot side maintained at 70-75°C with the temperature difference across the TEC maintained at around 20°C.

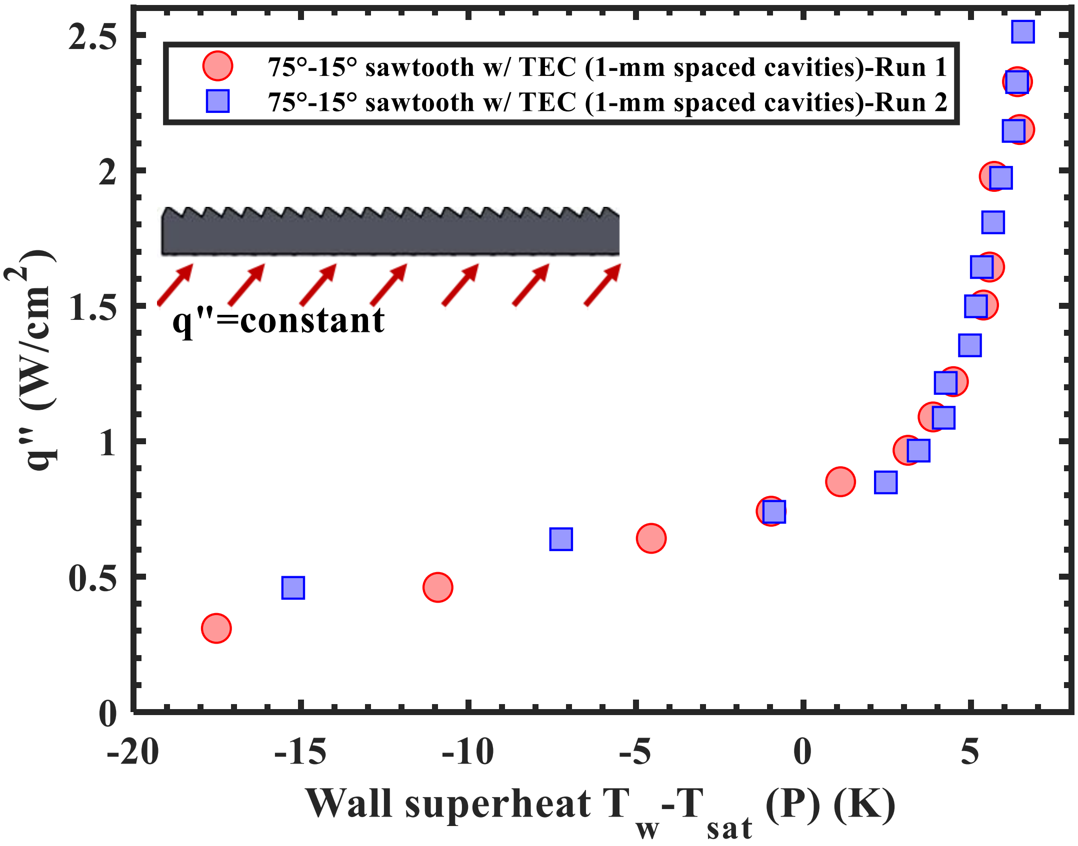

Figure 52: Tight agreement observed in the boiling curve between two different runs conducted under identical conditions

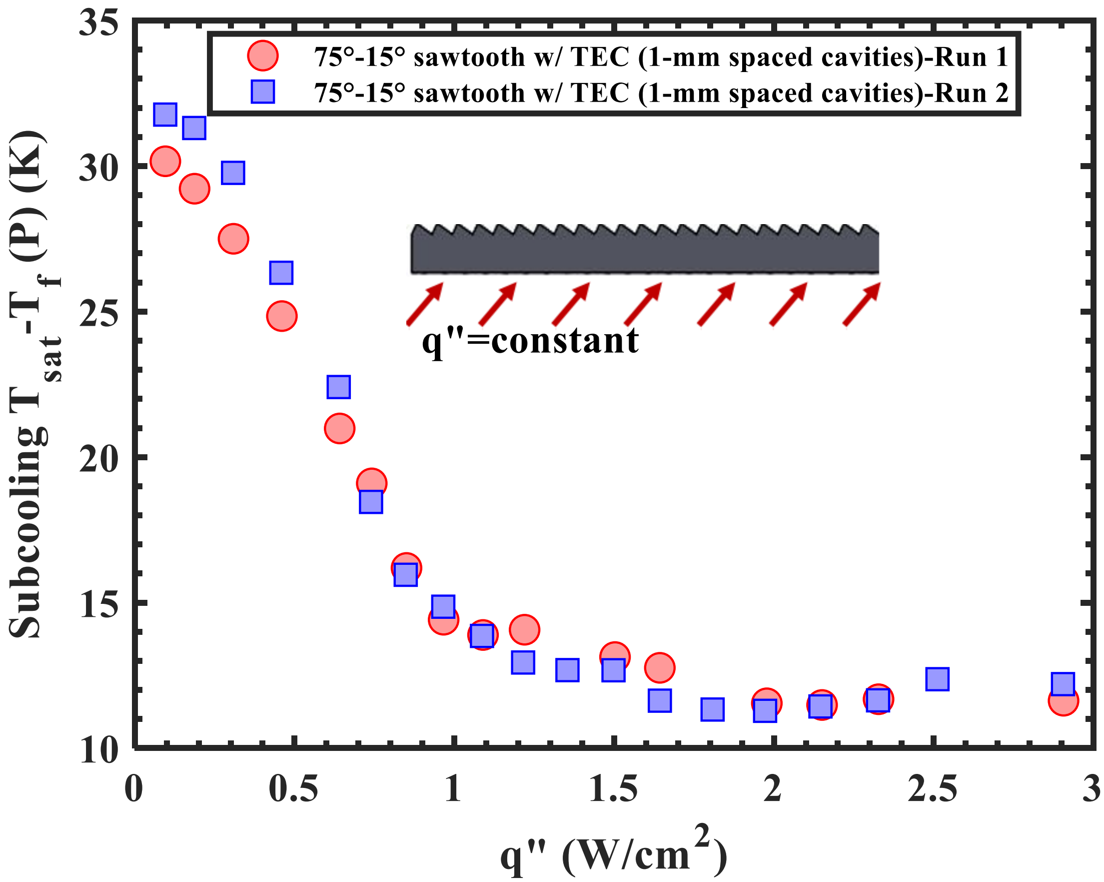

Figure 53: Bulk fluid subcooling data obtained during the experimental runs showing close agreement

However, the TEC's performance was not reliable as it required heat dissipation with bulky devices on the hot side to provide higher Watts of cooling. In addition, operating the TEC for multiple tests resulted in significant wear-and-tear of the electrical leads on the device.

Cold spot with Waterblock

A similar hypothesis was tested with a waterblock attached to a chiller to replicate low temperature. The boiling curve shifted to the right when the waterblock was used as shown in Figure 54. However, clear imagery of the bubbles migrating to the cold spot could not be obtained due to low liquid inventory after the onset of the nucleate boiling process. Moreover, the cavities closest to the waterblock on either side nucleated only at higher heat fluxes (>2.5 W/cm^2). This result suggests that the fluid close to the cold spot experienced higher subcooling conditions, suppressing nucleation from the nearby cavities. The summary of the waterblock experiments is presented in Table 11.

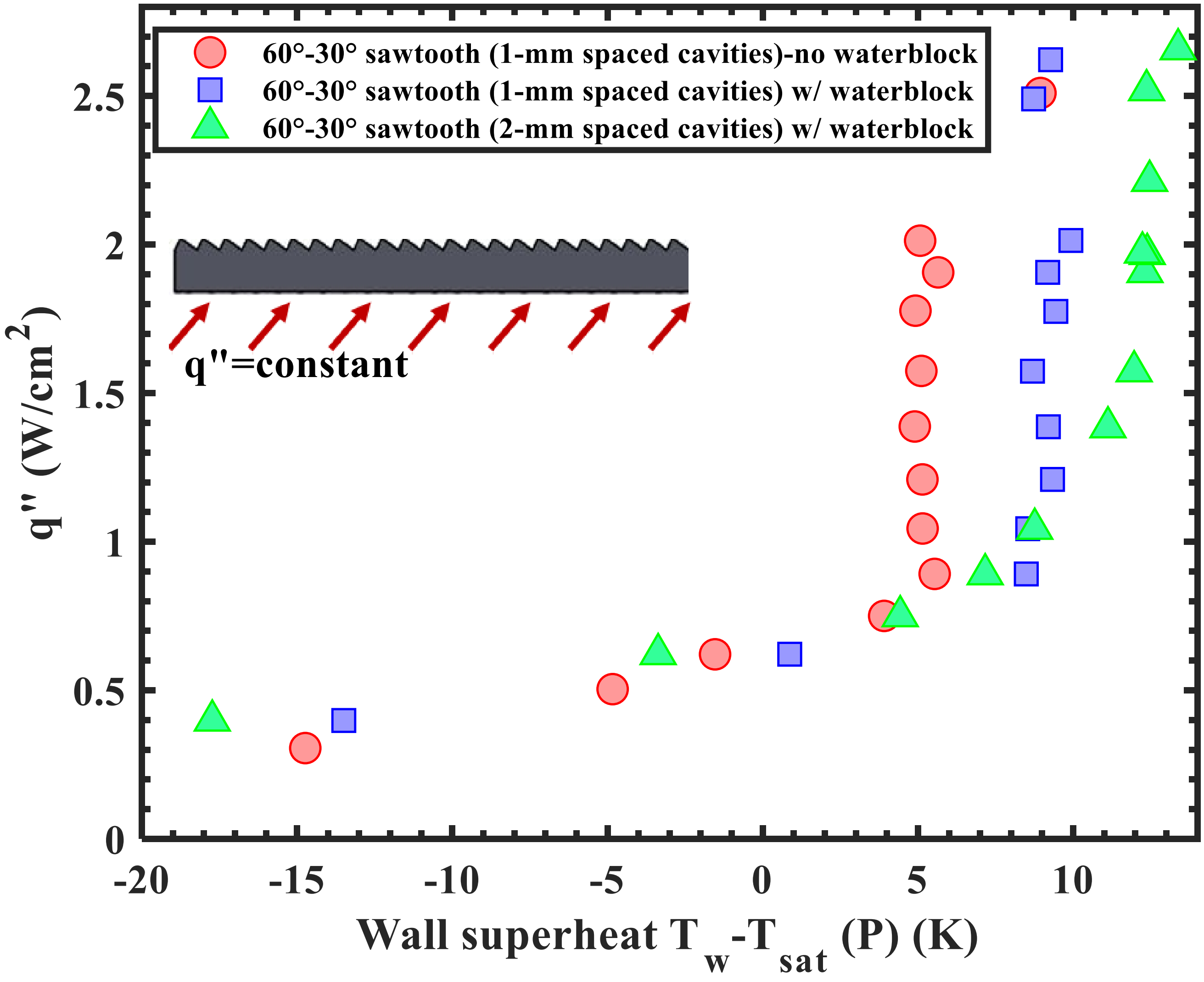

Figure 54: Effect of waterblock on the boiling curve along with nucleation site density

Table 11: Summary of the results of the waterblock and nucleation site density

Test surface and condition	**Waterblock Temperature Range (°C)**	**Subcooling (°C)**
60°-30° sawtooth, long with 1mm-spaced cavities (with waterblock)	2.13-3.7	21.24-24.5
60°-30° sawtooth, long with 2mm-spaced cavities (with waterblock)	3-4.8	22.5-24.7
60°-30° sawtooth, long with 1mm-spaced cavities (no waterblock)	-	22.7-24.6

Conclusions

The tests with the thermoelectric cooler and waterblock provided interesting insight into the initial hypothesis of nucleation, departure, and migration of vapor bubbles towards a cold spot.

1. Nucleation – While most cavities nucleated during the thermoelectric cooler experimental runs, the cavities close to the waterblock showed suppressed nucleation. This observation is in line with expectations, considering the waterblock's significantly lower temperature (~2-4°C) compared to the thermoelectric cooler (20°C).
2. Departure – Similar to the observations made in the upward-facing surfaces section in Chapter 3, the vapor bubble's direction was influenced close to the surface by the microstructure. As the bubble departed from the surface, buoyancy forces influenced the vapor bubble strongly

enough to change its path to nearly vertical within the frame of view. This result was in line with expectations and did not impact the overall hypothesis.

3. Migration – The migration of vapor bubbles towards the cold spot was the most difficult observation to achieve due to the low liquid inventory in the borosilicate tube. As the heat flux approached the onset of nucleate boiling, nucleation from the cavities produced enough vapor to form a column in the square tube. The column of vapor meant that vapor bubbles could not reach the cold spot, as they collapsed at the liquid-vapor interface. Detailed information on the low liquid inventory in the tube is discussed in the section on "Geometry Effects" in Chapter 3. While the thermoelectric cooler could not dissipate sufficient heat to influence this phenomenon, the waterblock achieved temperatures low enough to condense the produced vapor at low heat flues (<1.4 W/cm^2). However, nucleation was suppressed in cavities closest to the waterblock on either side. Unfortunately, it can be inferred that vapor bubbles from these cavities are precisely the ones most likely to complete migration to a cold spot, given their proximity. Though these cavities eventually nucleated at higher heat fluxes (>1.7 W/cm^2), vapor production at these fluxes was high enough to form a column of vapor in the tube.

The issues discussed above are the fundamental reasons why vapor bubble motion towards the cold spot remains a hypothesis.

Implications for the microgravity experiment

As a result of these preliminary observations with a single cold spot, the requirements for the microgravity experiments were modified to two cold spots. A single, central heated zone with a finite length will ensure better control over vapor formation as well. In addition, the cold spots will be placed sufficiently far enough from the heating zone to ensure the bulk fluid is influenced without suppressing nucleation from the cavities. It is expected that these modifications in a microgravity environment would provide improved data to validate passive vapor mobility from the microstructure.